SIAM J. SCI. COMPUT.
Vol. 41, No. 4, pp. B694–B720

A RELAXED PHYSICAL FACTORIZATION PRECONDITIONER FOR MIXED FINITE ELEMENT COUPLED POROMECHANICS*

MATTEO FRIGO†, NICOLA CASTELLETTO‡, AND MASSIMILIANO FERRONATO§

Abstract. In this paper, we introduce a relaxed physical factorization (RPF) preconditioner for the efficient iterative solution of the linearized algebraic system arising from the mixed finite element discretization of coupled poromechanics equations. The preconditioner is obtained by using a proper factorization of the 3×3 block matrix and setting a relaxation parameter α. The preconditioner is inspired by the relaxed dimensional factorization introduced by Benzi et al. [*J. Comput. Phys.*, 230 (2011), pp. 6185–6202; *Comput. Methods Appl. Mech. Engrg.*, 300 (2016), pp. 129–145]. A stable algorithm is advanced to compute the optimal value of α, along with a lower bound to control the possible ill-conditioning of the α dependent inner blocks. Numerical experiments in both theoretical benchmarks and real-world applications are presented and discussed to investigate the RPF properties, performance, and robustness.

Key words. preconditioning, Krylov subspace methods, mixed finite elements, poromechanics

AMS subject classifications. 65F10, 65F08, 65N30

DOI. 10.1137/18M120645X

1. Introduction.

We consider the solution of the Biot poroelasticity equations governing coupled Darcy flow and quasi-static mechanical deformation in a porous medium [10]. For a given bounded closed domain $\overline{\Omega} = \Omega \cup \Gamma \in \mathbb{R}^3$ with Ω an open set and Γ its boundary, time interval $\mathcal{I} = (0, t_{\max}]$, and volumetric fluid source s, a well-established mixed three-field formulation of Biot's initial/boundary value problem [25, 42, 48, 49, 35, 22, 30, 12, 4, 34, 51, 13, 31, 32] consists of finding the displacement vector field $\boldsymbol{u} : \overline{\Omega} \times \mathcal{I} \to \mathbb{R}^3$, the Darcy velocity $\boldsymbol{q} : \overline{\Omega} \times \mathcal{I} \to \mathbb{R}^3$, and the excess pore pressure $p : \overline{\Omega} \times \mathcal{I} \to \mathbb{R}$ that satisfy

$$-\operatorname{div} \boldsymbol{\sigma}(\boldsymbol{u}, p) = \mathbf{0} \qquad \text{in } \Omega \times \mathcal{I} \qquad \text{(linear momentum balance)}, \tag{1.1a}$$

$$\mu \boldsymbol{\kappa}^{-1} \cdot \boldsymbol{q} + \nabla p = 0 \qquad \text{in } \Omega \times \mathcal{I} \qquad \text{(Darcy's law)}, \tag{1.1b}$$

$$\dot{\xi}(\boldsymbol{u}, p) + \operatorname{div} \boldsymbol{q} = s \qquad \text{in } \Omega \times \mathcal{I} \qquad \text{(mass balance)}. \tag{1.1c}$$

Here, $\boldsymbol{\sigma} = (\mathbf{C} : \nabla^s \boldsymbol{u} - bp\mathbf{1})$ is the total Cauchy stress tensor, with $\nabla^s = \frac{1}{2}(\nabla + \nabla^T)$ the symmetric gradient operator, $\mathbf{C}$ the rank-4 elasticity tensor, b the Biot coefficient, and $\mathbf{1}$ the rank-2 identity tensor; μ and $\boldsymbol{\kappa}$ are the fluid viscosity and the rank-2 permeability tensor, respectively; $\xi = (b \operatorname{div} \boldsymbol{u} + \frac{1}{M} p)$ is the fluid content increment, with M the Biot modulus. In (1.1c) the superposed dot, $\dot{(\,)}$, is used to denote a

*Submitted to the journal's Computational Methods in Science and Engineering section August 9, 2018; accepted for publication (in revised form) May 7, 2019; published electronically July 11, 2019.

https://doi.org/10.1137/18M120645X

Funding: This work was supported by the University of Padova project "Methods and Algorithms for the Simulation of Flow and Mechanical Processes in Porous Media". Portions of this work were performed under the auspices of the U.S. Department of Energy by Lawrence Livermore National Laboratory under contract DE-AC52-07NA27344.

†Department ICEA, University of Padova, Padova, Italy (matteo.frigo.3@phd.unipd.it).

‡Atmospheric, Earth and Energy Division, Lawrence Livermore National Laboratory, Livermore, CA 94550 (castelletto1@llnl.gov).

§Corresponding author. Department ICEA, University of Padova, Padova, Italy (ferronat@dmsa.unipd.it).

derivative with respect to time. Introducing two disjoint partitions of the domain boundary such that $\Gamma = \overline{\Gamma_u^D \cup \Gamma_\sigma^N} = \overline{\Gamma_p^D \cup \Gamma_q^N}$, we assume, without loss of generality, homogeneous Dirichlet boundary conditions $\boldsymbol{u} = \boldsymbol{0}$ on $\Gamma_u^D \times \mathcal{I}$ and homogeneous Neumann conditions $\boldsymbol{q} \cdot \boldsymbol{n} = 0$ on $\Gamma_q^N \times \mathcal{I}$, along with Neumann conditions $\boldsymbol{\sigma} \cdot \boldsymbol{n} = \boldsymbol{t}^N$ on $\Gamma_\sigma^N \times \mathcal{I}$ and Dirichlet conditions $p = p^D$ on $\Gamma_p^D \times \mathcal{I}$, where $\boldsymbol{n}$ is the outer normal vector for Γ. Appropriate initial conditions $\boldsymbol{u}_0$, $\boldsymbol{q}_0$, and p_0 complete the formulation.

Let $\boldsymbol{H}_0^1(\Omega)$ denote the Sobolev space of vector functions satisfying displacement homogeneous Dirichlet conditions over Γ_u^D and whose first derivatives are square-integrable, i.e., they belong to $L^2(\Omega)$; and let $\boldsymbol{H}_0(\mathrm{div};\Omega)$ be the Sobolev space of vector functions with square-integrable divergence satisfying homogeneous Neumann conditions over Γ_q^N. For the analysis of the well-posedness of the Biot continuous problem (1.1) in weak form based on the displacement-velocity-pressure formulation the reader is referred to [42]. Let $\boldsymbol{\mathcal{U}}^h \subset \boldsymbol{H}_0^1(\Omega)$, $\boldsymbol{\mathcal{Q}}^h \subset \boldsymbol{H}_0(\mathrm{div};\Omega)$, $\mathcal{P}^h \subset L^2(\Omega)$ denote finite-dimensional subspaces. The semidiscrete variational statement of (1.1) reads as follows: for each $t \in \mathcal{I}$, find $\{\boldsymbol{u}^h(t), \boldsymbol{q}^h(t), p^h(t)\} \in \boldsymbol{\mathcal{U}}^h \times \boldsymbol{\mathcal{Q}}^h \times \mathcal{P}^h$ such that

$$(\nabla^s \boldsymbol{\eta}, \mathbf{C}_{\mathrm{dr}} : \nabla^s \boldsymbol{u}^h)_\Omega - (\mathrm{div}\ \boldsymbol{\eta}, b p^h)_\Omega = \int_{\Gamma_\sigma^N} \boldsymbol{\eta} \cdot \boldsymbol{t}^N \ \mathrm{d}\Gamma \qquad \forall \boldsymbol{\eta} \in \boldsymbol{\mathcal{U}}^h, \tag{1.2a}$$

$$(\boldsymbol{\psi}, \mu \boldsymbol{\kappa}^{-1} \cdot \boldsymbol{q}^h)_\Omega - (\mathrm{div}\ \boldsymbol{\psi}, p^h)_\Omega = -\int_{\Gamma_p^D} \boldsymbol{\psi} \cdot \boldsymbol{n} p^D \ \mathrm{d}\Gamma \qquad \forall \boldsymbol{\psi} \in \boldsymbol{\mathcal{Q}}^h, \tag{1.2b}$$

$$(b\ \mathrm{div}\ \dot{\boldsymbol{u}}^h, \chi)_\Omega + (\mathrm{div}\ \boldsymbol{q}^h, \chi)_\Omega + (\chi, M^{-1} \dot{p}^h)_\Omega = (\chi, s)_\Omega \qquad \forall \chi \in \mathcal{P}^h, \tag{1.2c}$$

where $(\cdot,\cdot)_\Omega$ represents the L^2-inner products of scalar functions in $L^2(\Omega)$, vector functions in $[L^2(\Omega)]^3$, or second-order tensor functions in $[L^2(\Omega)]^{3\times 3}$, as appropriate.

Let $\boldsymbol{u}^h = \sum_i u_i \boldsymbol{\eta}_i$, $\boldsymbol{q}^h = \sum_j q_j \boldsymbol{\psi}_j$, and $p^h = \sum_k p_k \chi_k$, where $\{\boldsymbol{\eta}_i\}$, $\{\boldsymbol{\psi}_j\}$, and $\{\chi_k\}$ are sets of basis functions for subspaces $\boldsymbol{\mathcal{U}}^h$, $\boldsymbol{\mathcal{Q}}^h$, and $\mathcal{P}^h$, respectively. Hence, the matrix form of the variational problem (1.2) reads

$$\begin{bmatrix} K & 0 & -Q \\ 0 & A & -B \\ 0 & B^T & 0 \end{bmatrix} \begin{bmatrix} \mathbf{u} \\ \mathbf{q} \\ \mathbf{p} \end{bmatrix} + \begin{bmatrix} 0 & 0 & 0 \\ 0 & 0 & 0 \\ Q^T & 0 & P \end{bmatrix} \begin{bmatrix} \dot{\mathbf{u}} \\ \dot{\mathbf{q}} \\ \dot{\mathbf{p}} \end{bmatrix} = \begin{bmatrix} \mathbf{f}_\sigma^N \\ \mathbf{g}_p^D \\ \mathbf{h}_s \end{bmatrix} \tag{1.3}$$

with $\mathbf{u}$, $\mathbf{q}$, and $\mathbf{p}$ the coefficient vectors required to expand the discrete displacement, velocity, and pressure fields in terms of the respective basis functions. In (1.3), K is the classical small displacement stiffness matrix, A is the (scaled) velocity mass matrix, P is the (scaled) pressure mass matrix, Q is the poromechanical coupling block, B is the Gram matrix, and vectors $\mathbf{f}_\sigma^N$, $\mathbf{g}_p^D$, and $\mathbf{h}_s$ come from the integration of the total traction Neumann conditions, the pressure Dirichlet boundary conditions, and the source term, respectively, with $\{\boldsymbol{\eta}_i, \boldsymbol{\eta}_j\}$, $\{\boldsymbol{\psi}_i, \boldsymbol{\psi}_j\}$, and $\{\chi_i, \chi_j\}$ ranging over the bases for $\boldsymbol{\mathcal{U}}^h$, $\boldsymbol{\mathcal{Q}}^h$, and $\mathcal{P}^h$:

$$[K]_{ij} = (\nabla^s \boldsymbol{\eta}_i, \mathbf{C}_{\mathrm{dr}} : \nabla^s \boldsymbol{\eta}_j)_\Omega \qquad \forall (i,j) \in \{1,\dots,n_u\} \times \{1,\dots,n_u\}, \tag{1.4a}$$

$$[A]_{ij} = (\boldsymbol{\psi}_i, \mu \boldsymbol{\kappa}^{-1} \cdot \boldsymbol{\psi}_j)_\Omega \qquad \forall (i,j) \in \{1,\dots,n_q\} \times \{1,\dots,n_q\}, \tag{1.4b}$$

$$[P]_{ij} = (\chi_i, M^{-1} \chi_j)_\Omega \qquad \forall (i,j) \in \{1,\dots,n_p\} \times \{1,\dots,n_p\}, \tag{1.4c}$$

$$[Q]_{ij} = (\mathrm{div}\ \boldsymbol{\eta}_i, b \chi_j)_\Omega \qquad \forall (i,j) \in \{1,\dots,n_u\} \times \{1,\dots,n_p\}, \tag{1.4d}$$

$$[B]_{ij} = (\mathrm{div}\ \boldsymbol{\psi}_i, \chi_j)_\Omega \qquad \forall (i,j) \in \{1,\dots,n_q\} \times \{1,\dots,n_p\}, \tag{1.4e}$$

$$[\mathbf{f}_\sigma^N]_i = \int_{\Gamma_\sigma^N} \boldsymbol{\eta}_i \cdot \boldsymbol{t}^N \ \mathrm{d}\Gamma \qquad \forall i \in \{1,\dots,n_u\}, \tag{1.4f}$$

$$[\mathbf{g}_p^D]_i = -\int_{\Gamma_p^D} \boldsymbol{\psi}_i \cdot \boldsymbol{n} p^D \, \mathrm{d}\Gamma \qquad \forall i \in \{1, \dots, n_q\}, \tag{1.4g}$$

$$[\mathbf{h}_s]_i = (\chi_i, s)_\Omega \qquad \forall i \in \{1, \dots, n_p\}, \tag{1.4h}$$

with $n_u = \dim(\boldsymbol{\mathcal{U}}^h)$, $n_q = \dim(\boldsymbol{\mathcal{Q}}^h)$, and $n_p = \dim(\mathcal{P}^h)$. Finally, the system of differential-algebraic equations (1.3) is numerically integrated in time by the classic θ-method. Advancing the solution from discrete time level t_n to t_{n+1} requires the solution of the following linear algebraic system:

$$\mathbf{A}\mathbf{x} = \mathbf{b} \quad \text{with} \quad \mathbf{A} = \begin{bmatrix} K & 0 & -Q \\ 0 & A & -B \\ Q^T & \gamma B^T & P \end{bmatrix}, \quad \mathbf{x} = \begin{bmatrix} \mathbf{u}_{n+1} \\ \mathbf{q}_{n+1} \\ \mathbf{p}_{n+1} \end{bmatrix}, \quad \mathbf{b} = \begin{bmatrix} \mathbf{f} \\ \mathbf{g} \\ \mathbf{h} \end{bmatrix}, \tag{1.5}$$

where

$$\mathbf{f} = \left[\mathbf{f}_{\sigma,n+1}^N - \frac{1-\theta}{\theta}(K\mathbf{u}_n - Q\mathbf{p}_n - \mathbf{f}_{\sigma,n}^N) \right], \tag{1.6a}$$

$$\mathbf{g} = \left[\mathbf{g}_{p,n+1}^D - \frac{1-\theta}{\theta}(A\mathbf{q}_n - B\mathbf{p}_n - \mathbf{g}_{p,n}^D) \right], \tag{1.6b}$$

$$\mathbf{h} = [(\Delta t_n - \gamma)(\mathbf{h}_{s,n} - B^T\mathbf{q}_n) + Q^T\mathbf{u}_n + P\mathbf{p}_n + \gamma\mathbf{h}_{s,n+1}], \tag{1.6c}$$

$$\gamma = \theta \Delta t_n, \tag{1.6d}$$

with Δt_n the time integration step size $(t_{n+1} - t_n)$ and θ a real parameter $(1/2 \leq \theta \leq 1)$. Notice that the matrix $\mathbf{A}$ in (1.5) is nonsymmetric. Though it could be easily symmetrized, in this work we prefer keeping the nonsymmetry because (i) the symmetric form would be indefinite anyway, and (ii) with the structure (1.5) the Schur complement computed with respect to the third line turns out to be positive definite, thus allowing for some important theoretical developments.

Introducing a single conforming computation grid, we consider as in [16] a spatial discretization that relies on the continuous piecewise trilinear displacement finite element space ($\mathbb{Q}_1$), the lowest-order Raviart–Thomas finite element space ($\mathbb{RT}_0$), and the finite element space of piecewise constant functions ($\mathbb{P}_0$) for $\boldsymbol{\mathcal{U}}^h$, $\boldsymbol{\mathcal{Q}}^h$, and $\mathcal{P}^h$, respectively. This choice allows for obtaining locally (elementwise) mass-conservative velocity fields and is robust with respect to strong contrasts in permeability tensors—an essential requirement, for example, in geoscience applications involving complex multiphase flow [36] or thermal convection [14]. Note that K and A are symmetric positive definite (SPD), while P is diagonal with nonnegative entries. We recognize that the $\mathbb{Q}_1$-$\mathbb{RT}_0$-$\mathbb{P}_0$ discretization does not intrinsically satisfy the inf-sup stability in the undrained limit [42, 51], i.e., for small time-step sizes in the presence of small permeability coefficients when $\frac{1}{M} \to 0$, i.e., when the porous medium consists of incompressible solid and fluid constituents. Whenever undrained conditions are approached a stabilization strategy must be introduced to ensure reliable numerical results. For instance, in [51] the authors propose using special face bubble functions that, based on a spectral equivalence relation, allow for eliminating the additional degrees of freedom via static condensation and recovering a 3×3 block linear system similar to $\mathbf{A}$. In this work we will restrict ourselves to drained configurations to avoid the need for stabilization—our computational experience suggests that this is often practically the case also for $\frac{1}{M} \to 0$ if physically meaningful time steps are chosen. Moreover, we observe also that the three-field formulation (1.2) might not address properly the mechanical locking due to a Poisson ratio close to 0.5. The applications we will consider in this work, however, are mainly connected with flow and deformation in geological media, where such a condition is usually rare.

Our focus here is on the solution of fully implicit linear systems of the form (1.5). In three-dimensional large-size practical applications, where sparse direct solvers are not an option, the availability of rapidly convergent iterative methods is key. Over the past decade and a half, a rich literature concerning the design of efficient iterative solvers has developed for the Biot problem based on a two-field (displacement-pressure) formulation. In particular, most of the efforts have been toward preconditioned Krylov solvers [7, 54, 9, 29, 55, 40, 1] and multigrid methods [26, 43, 27, 44]. As far as the $\mathbb{Q}_1$-$\mathbb{RT}_0$-$\mathbb{P}_0$ discretization is concerned, iterative solution schemes have been typically proposed adopting sequential-implicit approaches [35, 28, 2, 12, 11, 20, 21, 32] where the poromechanical equilibrium and the Darcy flow subproblem are addressed independently iterating until coupled convergence. In sequential approaches, suitable splitting strategies are necessary to warrant unconditional convergence. The most established algorithms build on the *fixed-stress* coupling scheme [37, 38, 46]. For unconditionally stable fully implicit simulation—also known as fully coupled or monolithic—fewer works have been published. Spectrally equivalent block diagonal preconditioners were first proposed in [42, 39] and further discussed in [52, 31]. Families of block preconditioners that combine physically based and fully algebraic arguments to construct various Schur complement approximations were proposed in [22, 16].

In this work we develop a new preconditioner, denoted as relaxed physical factorization (RPF), for the linear system (1.5) to accelerate the convergence of a nonsymmetric Krylov subspace method. This preconditioner is inspired by the relaxed dimensional factorization (RDF) introduced by Benzi et al. [6, 5] for the saddle-point problems arising from Navier–Stokes equations. A similar idea is used here by replacing the dimensional block matrix subdivision with the inherent physically based partitioning and extending the original formulation by taking into account the possible nonzero contribution from the (3,3)-block P. The preconditioned matrix eigenspectrum depends on a relaxation parameter α, whose optimal selection is obtained by an algorithm which ensures an automatic control of the possible ill-conditioning of α-dependent inner blocks. The paper is organized as follows. In section 2 the RPF preconditioner is derived from a splitting of $\mathbf{A}$. The eigenspectrum of the RPF preconditioned matrix is investigated to develop an algorithm for the optimal setting of the relaxation parameter α. Section 3 discusses the RPF computation and application, introducing two lower bounds for α in order to keep under control the possible ill-conditioning of the α-dependent inner blocks. The RPF performance and robustness is then investigated in section 4 with the aid of both classical theoretical benchmarks and real-world poromechanical applications. Finally, a few conclusive remarks close the paper in section 5.

2. Relaxed physical factorization preconditioner. We begin this section by deriving the RPF preconditioner for mixed finite element coupled poromechanics. First, consider the following two splittings for the system matrix $\mathbf{A}$:

$$\mathbf{A} = \begin{bmatrix} K & 0 & -Q \\ 0 & I_q & 0 \\ Q^T & 0 & P \end{bmatrix} + \begin{bmatrix} 0 & 0 & 0 \\ 0 & A - I_q & -B \\ 0 & \gamma B^T & 0 \end{bmatrix} = \mathbf{A}_1^M + \mathbf{A}_1^F, \tag{2.1a}$$

$$\mathbf{A} = \begin{bmatrix} K - I_u & 0 & -Q \\ 0 & 0 & 0 \\ Q^T & 0 & 0 \end{bmatrix} + \begin{bmatrix} I_u & 0 & 0 \\ 0 & A & -B \\ 0 & \gamma B^T & P \end{bmatrix} = \mathbf{A}_2^M + \mathbf{A}_2^F, \tag{2.1b}$$

with I_u and I_q the identity matrix in $\mathbb{R}^{n_u \times n_u}$ and $\mathbb{R}^{n_q \times n_q}$, respectively. From a physical point of view, matrix $\mathbf{A}_1^M$ corresponds to the discretization of a poromechanical equilibrium problem under undrained conditions, i.e., decoupled from fluid flow. Conversely, matrix $\mathbf{A}_2^F$ is representative of a Darcy problem in mixed form with no mechanical effects accounted for. Utilizing the splittings given in (2.1), the following physics-based alternating-type iteration can be defined:

$$\mathbf{A}_1^M \mathbf{x}^{k+\frac{1}{2}} = -\mathbf{A}_1^F \mathbf{x}^k + \mathbf{b}, \tag{2.2a}$$

$$\mathbf{A}_2^F \mathbf{x}^{k+1} = -\mathbf{A}_2^M \mathbf{x}^{k+\frac{1}{2}} + \mathbf{b}, \tag{2.2b}$$

where k denotes the iteration count, $k \in \{0, 1, \ldots\}$. Eliminating $\mathbf{x}^{k+\frac{1}{2}}$ from these leads to the stationary scheme

$$\mathbf{x}^{k+1} = \mathbf{G}\mathbf{x}^k + \mathbf{c} \tag{2.3}$$

with $\mathbf{G} = \mathbf{A}_2^{F,-1}\mathbf{A}_2^M\mathbf{A}_1^{M,-1}\mathbf{A}_1^F$ the iteration matrix and $\mathbf{c} = \mathbf{A}_2^{F,-1}(\mathbf{I} - \mathbf{A}_2^M\mathbf{A}_1^{M,-1})\mathbf{b}$. Here, $\mathbf{I}$ is the identity matrix of order $n_u + n_q + n_p$. The matrix $\mathbf{G}$ can be rewritten as

$$\begin{aligned} \mathbf{G} &= \mathbf{A}_2^{F,-1}\mathbf{A}_2^M\mathbf{A}_1^{M,-1}\mathbf{A}_1^F \\ &= (\mathbf{A}_2^{F,-1}\mathbf{A} - \mathbf{I})(\mathbf{A}_1^{M,-1}\mathbf{A} - \mathbf{I}) \\ &= \mathbf{I} - \mathbf{A}_2^{F,-1}(\mathbf{A}_1^M - \mathbf{A}_2^M)\mathbf{A}_1^{M,-1}\mathbf{A} \\ &= \mathbf{I} - \widetilde{\mathbf{M}}^{-1}\mathbf{A}, \end{aligned} \tag{2.4}$$

which provides the expression for the preconditioning matrix associated with the iteration scheme (2.3), namely, $\widetilde{\mathbf{M}} = \mathbf{A}_1^M(\mathbf{A}_1^M - \mathbf{A}_2^M)^{-1}\mathbf{A}_2^F$. Substituting the expressions for $\mathbf{A}_1^M$, $\mathbf{A}_2^M$, and $\mathbf{A}_2^F$ yields

$$\widetilde{\mathbf{M}} = \begin{bmatrix} K & 0 & -Q \\ 0 & I_q & 0 \\ Q^T & 0 & P \end{bmatrix} \begin{bmatrix} I_u & 0 & 0 \\ 0 & I_q & 0 \\ 0 & 0 & P^{-1} \end{bmatrix} \begin{bmatrix} I_u & 0 & 0 \\ 0 & A & -B \\ 0 & \gamma B^T & P \end{bmatrix}. \tag{2.5}$$

We note that the definition of $\widetilde{\mathbf{M}}$ involves the inverse of the (scaled) pressure mass matrix. Remembering that the entries of P are proportional to $\frac{1}{M}$, with M the Biot modulus, the P matrix could be singular, or it gets close to being so, when both the solid and fluid constituents are almost incompressible. Hence matrix P cannot be inverted in a numerically stable way. In order to avoid this drawback, many strategies have been used, such as adding some regularization terms [3] or trivially avoiding computing P^{-1} [16]. In this paper, we propose to replace the matrix P by the identity matrix I_p in $\mathbb{R}^{n_p \times n_p}$ scaled by a real relaxation parameter $\alpha > 0$. Doing so, the proposed preconditioner $\mathbf{M}$ is derived from the following factorization:

$$\mathbf{M} = \frac{1}{\alpha}\mathbf{M}_1\mathbf{M}_2 = \frac{1}{\alpha}\begin{bmatrix} K & 0 & -Q \\ 0 & \alpha I_q & 0 \\ Q^T & 0 & \alpha I_p \end{bmatrix} \begin{bmatrix} \alpha I_u & 0 & 0 \\ 0 & A & -B \\ 0 & \gamma B^T & \alpha I_p \end{bmatrix} = \begin{bmatrix} K & -\frac{\gamma}{\alpha}QB^T & -Q \\ 0 & A & -B \\ Q^T & \gamma B^T & \alpha I_p \end{bmatrix}, \tag{2.6}$$

A similar approach was already introduced in the numerical solution of the saddle-point matrices arising from Navier–Stokes problems [6]. Comparing (1.5) with (2.6), the difference $\mathbf{R}$ between $\mathbf{M}$ and $\mathbf{A}$ is

$$\mathbf{R} = \mathbf{M} - \mathbf{A} = \begin{bmatrix} 0 & -\frac{\gamma}{\alpha} Q B^T & 0 \\ 0 & 0 & 0 \\ 0 & 0 & \alpha I_p - P \end{bmatrix}. \tag{2.7}$$

Looking at (2.7), it can be heuristically observed that α should satisfy two conflicting requirements: (i) to be as close as possible to the coefficients of P and (ii) to be as large as possible in order to reduce the contribution arising from the (1,2) block of $\mathbf{R}$.

2.1. Spectral analysis. The objective of the analysis developed in this section is to provide information about the dependency on α of the eigenvalues of the preconditioned matrix $\mathbf{T} = \mathbf{M}^{-1}\mathbf{A}$. Recalling the definition (2.6), the RPF preconditioner $\mathbf{M}^{-1}$ can be written as

$$\mathbf{M}^{-1} = \alpha \mathbf{M}_2^{-1} \mathbf{M}_1^{-1}, \tag{2.8}$$

where the inverses of $\mathbf{M}_1$ and $\mathbf{M}_2$ read

$$\mathbf{M}_1^{-1} = \frac{1}{\alpha} \begin{bmatrix} \alpha \hat{K}^{-1} & 0 & \hat{K}^{-1} Q \\ 0 & I_q & 0 \\ -Q^T \hat{K}^{-1} & 0 & I_p - \frac{1}{\alpha} \hat{S}_K \end{bmatrix}, \quad \mathbf{M}_2^{-1} = \frac{1}{\alpha} \begin{bmatrix} I_u & 0 & 0 \\ 0 & \alpha \hat{A}^{-1} & \hat{A}^{-1} B \\ 0 & -\gamma B^T \hat{A}^{-1} & I_p - \frac{1}{\alpha} \hat{S}_A \end{bmatrix}, \tag{2.9}$$

with the definitions that follow for the inner blocks:

$$\hat{K} = K + \frac{1}{\alpha} Q Q^T, \tag{2.10a}$$

$$\hat{A} = A + \frac{\gamma}{\alpha} B B^T, \tag{2.10b}$$

$$\hat{S}_K = Q^T \hat{K}^{-1} Q, \tag{2.10c}$$

$$\hat{S}_A = \gamma B^T \hat{A}^{-1} B. \tag{2.10d}$$

Details on the derivation of $\mathbf{M}_1^{-1}$ and $\mathbf{M}_2^{-1}$ are given in Appendix A.

First, the following important result is provided.

THEOREM 2.1. *Let* $\mathbf{A}$ *and* $\mathbf{M}$ *be the matrices in* (1.5) *and* (2.6). *Then,* $n_u + n_q$ *eigenvalues of the preconditioned matrix* $\mathbf{T} = \mathbf{M}^{-1}\mathbf{A}$ *are* 1 *and* n_p *eigenvalues are those of*

$$Z_\alpha = \frac{1}{\alpha}(\hat{S}_K + \hat{S}_A + P) - \frac{1}{\alpha^2}(2\hat{S}_K \hat{S}_A + \hat{S}_K P + P \hat{S}_A) + \frac{1}{\alpha^3}(\hat{S}_K P \hat{S}_A). \tag{2.11}$$

Proof. Using (2.7) and (2.9), matrix $\mathbf{T}$ reads

$$\mathbf{T} = \mathbf{M}^{-1}\mathbf{A} = \mathbf{I} - \mathbf{M}^{-1}\mathbf{R} = \mathbf{I} - \alpha \mathbf{M}_2^{-1} \mathbf{M}_1^{-1} \mathbf{R} = \mathbf{I} - \begin{bmatrix} 0 & \mathbf{T}_{12} \\ 0 & \mathbf{T}_{22} \end{bmatrix}, \tag{2.12}$$

where $\mathbf{T}_{12} \in \mathbb{R}^{n_u \times (n_q + n_p)}$, $\mathbf{T}_{22} \in \mathbb{R}^{(n_q+n_p)\times(n_q+n_p)}$, and

$$\mathbf{T}_{12} = \begin{bmatrix} -\frac{\gamma}{\alpha} \hat{K}^{-1} Q B^T & \frac{1}{\alpha} \hat{K}^{-1} Q \left(\alpha I_p - P\right) \end{bmatrix}, \tag{2.13a}$$

$$\mathbf{T}_{22} = \frac{1}{\alpha} \begin{bmatrix} \frac{\gamma}{\alpha} \hat{A}^{-1} B \hat{S}_K B^T & \hat{A}^{-1} B \left(I_p - \frac{1}{\alpha} \hat{S}_K\right) (\alpha I_p - P) \\ \frac{\gamma}{\alpha} \left(I_p - \frac{1}{\alpha} \hat{S}_A\right) \left(\hat{S}_K B^T\right) & \left(I_p - \frac{1}{\alpha} \hat{S}_A\right) \left(I_p - \frac{1}{\alpha} \hat{S}_K\right) (\alpha I_p - P) \end{bmatrix}. \tag{2.13b}$$

Matrix $\mathbf{T}_{22}$ can also be written as $\alpha^{-2}\mathbf{X}\mathbf{Y}^T$, where $\mathbf{X}, \mathbf{Y} \in \mathbb{R}^{(n_q+n_p)\times n_p}$ and

$$\mathbf{X} = \begin{bmatrix} \hat{A}^{-1}B \\ \frac{1}{\alpha}\left(\alpha I_p - \hat{S}_A\right) \end{bmatrix}, \quad \mathbf{Y} = \begin{bmatrix} \gamma \hat{S}_K B^T \\ \left(\alpha I_p - \hat{S}_K\right)(\alpha I_p - P) \end{bmatrix}. \tag{2.14}$$

Hence, $\mathbf{T}_{22}$ has at most rank n_p. According to Theorem 1.3.22 in [33], the n_p nonzero eigenvalues of $\alpha^{-2}\mathbf{X}\mathbf{Y}^T$ are those of $\alpha^{-2}\mathbf{Y}^T\mathbf{X}$. We can write

$$\frac{1}{\alpha^2}\mathbf{Y}^T\mathbf{X} = I_p - Z_\alpha \tag{2.15}$$

with Z_α defined in (2.11). Denoting with μ_i, $i = 1, \ldots, n_p$, the eigenvalues of Z_α, from (2.12) we can conclude that the eigenvalues of $\mathbf{T}$ are either 1, with multiplicity $n_u + n_q$, or μ_i. ∎

According to Theorem 2.1, the preconditioned matrix $\mathbf{M}^{-1}\mathbf{A}$ has only n_p nonunitary eigenvalues which are those of matrix Z_α in (2.11). Additional insight on such eigenvalues is given by the result that follows.

THEOREM 2.2. *Let $S_K = Q^T K^{-1} Q$ and $S_A = \gamma B^T A^{-1} B$. Then, the eigenvalues μ_i of Z_α in* (2.11) *are*

$$\mu_i = \frac{\alpha\lambda_i}{1 + \alpha\lambda_i}, \qquad i = 1, \ldots, n_p, \tag{2.16}$$

where λ_i satisfies the generalized eigenproblem:

$$S\mathbf{w}_i = \lambda_i \left[\alpha\left(\alpha I_p - P\right) + S_K S_A\right]\mathbf{w}_i \tag{2.17}$$

with $S = P + S_K + S_A$.

Proof. Using the matrices S_K, S_A, and S, it is possible to obtain an equivalent expression for Z_α:

$$Z_\alpha = \alpha\left(\alpha I_p + S_K\right)^{-1} S \left(\alpha I_p + S_A\right)^{-1}. \tag{2.18}$$

Details on the algebraic developments leading to (2.18) are provided in Appendix B. It can be immediately observed from (2.18) that Z_α is similar to $\alpha(\alpha I_p + S_A)^{-1}(\alpha I_p + S_K)^{-1}S$. Hence, the eigenvalues μ_i satisfy the generalized eigenproblem:

$$\begin{aligned} \alpha S\mathbf{w}_i &= \mu_i \left(\alpha I_p + S_K\right)\left(\alpha I_p + S_A\right)\mathbf{w}_i \\ &= \mu_i \left[\alpha\left(\alpha I_p - P\right) + \alpha S + S_K S_A\right]\mathbf{w}_i, \end{aligned} \tag{2.19}$$

which can be rewritten in the form

$$S\mathbf{w}_i = \frac{\mu_i}{\alpha\left(1 - \mu_i\right)}\left[\alpha\left(\alpha I_p - P\right) + S_K S_A\right]\mathbf{w}_i. \tag{2.20}$$

Therefore, $\lambda_i = \mu_i/[\alpha(1 - \mu_i)]$ and the result (2.16) follows immediately. ∎

Theorem 2.2 can be used to analyze the eigenspectrum of Z_α. In particular, the following important result holds true.

COROLLARY 2.3. *If $\alpha \geq ||P||_\infty$, then $\mu_i \in \mathbb{R}$ and $0 < \mu_i < 1$.*

Proof. The matrices S and $(S_K S_A)$ are positive definite, as sum and product of SPD matrices. If $\alpha \geq ||P||_\infty$, then $(\alpha I_p - P)$ is positive semidefinite, and λ_i is real and positive. From (2.16), the thesis follows. ∎

The hypothesis of Corollary 2.3 provides a lower bound for α. Let the generalized eigenvector $\mathbf{w}_i$ corresponding to λ_i be such that $||\mathbf{w}_i||_2 = 1$. Then

$$\lambda_i = \frac{\mathbf{w}_i^T S \mathbf{w}_i}{\alpha^2 - \alpha \mathbf{w}_i^T P \mathbf{w}_i + \mathbf{w}_i^T S_K S_A \mathbf{w}_i}, \tag{2.21}$$

and in the limit toward the boundary of the existence domain for α we have

$$\lim_{\alpha \to \|P\|_\infty^+} \lambda_i = \bar{\lambda}_i(\|P\|_\infty), \quad \lim_{\|P\|_\infty \to 0} \bar{\lambda}_i = \frac{\mathbf{w}_i^T (S_K + S_A) \mathbf{w}_i}{\mathbf{w}_i^T S_K S_A \mathbf{w}_i}, \quad \lim_{\alpha \to \infty} \lambda_i = 0. \tag{2.22}$$

Recalling (2.16), for the eigenvalues of Z_α we obtain immediately

$$\lim_{\alpha \to \|P\|_\infty^+} \mu_i = \frac{\|P\|_\infty \bar{\lambda}_i}{1 + \|P\|_\infty \bar{\lambda}_i} = \overline{\mu}_i, \quad \lim_{\|P\|_\infty \to 0} \overline{\mu}_i = 0, \quad \lim_{\alpha \to +\infty} \mu_i = 0. \tag{2.23}$$

In summary, we can conclude that for $\alpha \geq \|P\|_\infty$ the eigenvalues of the preconditioned matrix $\mathbf{M}^{-1}\mathbf{A}$ have the following properties: (i) they are real and positive; (ii) they are either 1, with multiplicity $n_u + n_q$, or smaller than 1; (iii) the nonunitary eigenvalues tend to 0 for $\alpha \to \infty$ and to a finite value $\overline{\mu}_i$ for $\alpha \to \|P\|_\infty$; and (iv) $\overline{\mu}_i$ tends to 0 with $\|P\|_\infty$.

2.2. Optimal selection of the relaxation parameter. The objective is to select the relaxation parameter α so as to cluster as much as possible the eigenvalues of $\mathbf{M}^{-1}\mathbf{A}$, hence of Z_α, around 1. Following the arguments developed in [5] and using the result of Corollary 2.3, the relaxation parameter α should be selected as

$$\alpha_1 = \arg \min_{\alpha \geq \|P\|_\infty} \left(n_p - \operatorname{tr}\left[Z_\alpha \right] \right). \tag{2.24}$$

Finding analytically α_1 as in (2.24) can be an expensive task, because Z_α is a dense matrix. In order to make the practical computation of α_1 more affordable, S_K and S_A can be replaced by diagonal matrices. In the context of poromechanics, these approximations can be done on the basis of both physical and algebraic considerations. As far as S_K is concerned, it has been argued already in [55, 16] that it physically takes the role of the so-called fixed-stress matrix in one of the splitting schemes introduced for the sequential solution of a coupled poromechanical model [37, 38, 46, 2]. Following the notation introduced in section 1, (1.4h), we can effectively replace S_K with [16]:

$$[D_K^{(fs)}]_{ij} = (\chi_i, b^2 \zeta^{-1} \chi_j)_\Omega \qquad \forall (i,j) \in \{1, \ldots, n_p\} \times \{1, \ldots, n_p\}, \tag{2.25}$$

where ζ is a physical parameter denoting the bulk modulus, either volumetric or uniaxial according to the poromechanical model properties.

Remark 2.4. Castelletto, White, and Ferronato [16] have pointed out that the matrix $D_K^{(fs)}$ can also be computed in a fully algebraic way. Denoting by $R^{(i)}$ the $n_u^{(i)} \times n_u$ restriction operator such that

$$K^{(i)} = R^{(i)} K R^{(i),T} \tag{2.26}$$

is the submatrix of K made by the entries in the rows and columns with indices corresponding to the positions of the $n_u^{(i)}$ nonzeros in the ith column of Q, $Q^{(i)}$, the scalar quantity

$$\bar{\zeta}_i = Q^{(i),T} K^{(i),-1} Q^{(i)} \tag{2.27}$$

is equivalent to the value of ζ associated to the ith element of the partition defined in the domain Ω.

For the matrix S_A, a well-established approximation introduced in the context of the mixed finite solution of Darcy's flow, e.g., in [8] and references therein, consists of weighting a standard Laplacian by the Euclidean norm of the rows of A. Such an approach has also been used in the three-field poromechanical models [16]. Defining the lumped matrix $\widetilde{A}$ whose diagonal is given by

$$\operatorname{diag}(\widetilde{A}) = \left(a_1, a_2, \ldots, a_{n_q}\right), \qquad a_i = \left(\sum_{j=1}^{n_q} |A_{ij}|\right)^{1/2}, \qquad i \in \{1, \ldots, n_q\}, \tag{2.28}$$

matrix S_A is replaced by

$$D_A = \gamma \operatorname{diag}\left(B^T \widetilde{A}^{-1} B\right). \tag{2.29}$$

Remark 2.5. A similar idea could also be used for approximating S_K. Instead of using $D_K^{(fs)}$, the matrix

$$D_K = \operatorname{diag}\left\{Q^T \left[\operatorname{diag}(K)\right]^{-1} Q\right\} \tag{2.30}$$

can be employed, as suggested, for instance, in [50, 17] in the context of coupled poromechanics. When used for preconditioning purposes, however, such an approach usually does not prove overly effective [7, 24].

Recalling (2.18) and using the approximations D_K or $D_K^{(fs)}$ and D_A for S_K and S_A, respectively, the trace of Z_α can be written as

$$\operatorname{tr}[Z_\alpha] \simeq \sum_{i=1}^{n_p} \left[\frac{\alpha S^{(i)}}{\left(\alpha + {D_A}^{(i)}\right)\left(\alpha + {D_K}^{(i)}\right)}\right] = \sum_{i=1}^{n_p} \left[Z_\alpha^{(i)}\right], \tag{2.31}$$

where $S^{(i)} = P^{(i)} + D_K^{(i)} + D_A^{(i)}$, ${D_K}^{(i)}$ and ${D_A}^{(i)}$ is the ith entry of the diagonal approximations of S, S_K, and S_A, respectively. The optimal value α_1 for the relaxation parameter α therefore can be obtained by minimizing the function

$$\varphi(\alpha) = n_p - \sum_{i=1}^{n_p} \left[Z_\alpha^{(i)}\right] \tag{2.32}$$

with the aid of a Newton–Raphson scheme. However, $\varphi(\alpha)$ can have several relative maximum and minimum points, so recognizing the absolute minimum might be difficult. To avoid this drawback another criterion is proposed. Since for $\alpha \geq \|P\|_\infty$ we have that $\operatorname{tr}[Z_\alpha] < n_p$ (Corollary 2.3), then

$$\arg \min_{\alpha \geq \|P\|_\infty} \left(n_p - \operatorname{tr}[Z_\alpha]\right) = \arg \max_{\alpha \geq \|P\|_\infty} \left(\operatorname{tr}[Z_\alpha]\right). \tag{2.33}$$

Using again (2.31), we easily see that $\mathrm{tr}\,[Z_\alpha]$ is maximum when each entry $Z_\alpha^{(i)}$ is so. Simply studying the behavior of $Z_\alpha^{(i)}$ as a function of α, it is easy to observe that $Z_\alpha^{(i)}$ can have a unique maximum in $[\|P\|_\infty, +\infty[$ obtained by setting to zero the derivative with respect to α,

$$\alpha^2 - D_K^{(i)} D_A^{(i)} = 0 \quad \Rightarrow \quad \alpha = \sqrt{D_K^{(i)} D_A^{(i)}}, \qquad i = 1, \dots, n_p, \tag{2.34}$$

or the maximum of $Z_\alpha^{(i)}$ is at $\alpha = \|P\|_\infty$ if $\|P\|_\infty > \sqrt{D_K^{(i)} D_A^{(i)}}$. Assume that the values of $\sqrt{D_K^{(i)} D_A^{(i)}}$ are listed in ascending order and that the first n_P entries are smaller than $\|P\|_\infty$. Then, the least-square solution to the n_p conditions (2.34) trivially reads

$$\begin{aligned} \alpha_2 &= \frac{1}{n_p} \left(\sum_{i=n_P+1}^{n_p} \sqrt{D_K^{(i)} D_A^{(i)}} + n_P \|P\|_\infty \right) \\ &= \frac{1}{n_p} \left(\sqrt{\gamma} \sum_{i=n_P+1}^{n_p} \sqrt{D_K^{(i)} \tilde{D}_A^{(i)}} + n_P \|P\|_\infty \right), \end{aligned} \tag{2.35}$$

where $\tilde{D}_A^{(i)} = \gamma^{-1} D_A^{(i)}$ is introduced to highlight the dependency of α_2 on γ. Unlike (2.31), the estimate (2.35) allows us to compute α straightforwardly, without the need for solving the nonlinear equation (2.31).

To conclude this section, we analyze how the optimal value of α is expected to change with the physical and geometrical properties of the investigated problem. For the sake of simplicity, assume that the problem is homogeneous and discretized by a regular partition of characteristic size h. Recalling (2.25) and (2.29), the diagonal entries of D_K and D_A read

$$D_K^{(i)} \propto \frac{|\Omega^{(e)}|}{\zeta}, \qquad D_A^{(i)} \propto \frac{\kappa}{\mu} \frac{|\Omega^{(e)}|}{\overline{h}^2}, \tag{2.36}$$

where $|\Omega^{(e)}|$ is the elemental measure. Using (2.36) into (2.35), we have

$$\alpha_2 \propto \sqrt{\gamma} \sqrt{\frac{\kappa}{\mu\zeta}} |\Gamma^{(e)}| + \frac{1}{M} |\Omega^{(e)}| \tag{2.37}$$

with $|\Gamma^{(e)}|$ a measure of the elemental boundary. Equation (2.37) shows that the optimal value of α is expected to grow for soft and permeable materials, i.e., small ζ and large κ, and for coarse space and time discretizations, i.e., large $|\Gamma^{(e)}|$ and γ.

3. RPF computation and application. From an implementation point of view, it is convenient to start from the original equation (2.5) and replace the matrix P with αI_p. It is easy to verify that the RPF preconditioner can be equivalently written in the factored form:

$$\mathbf{M}^{-1} = \left(\begin{bmatrix} I_u & 0 & -\frac{1}{\alpha} Q \\ 0 & I_q & 0 \\ 0 & 0 & I_p \end{bmatrix} \begin{bmatrix} \hat{K} & 0 & 0 \\ 0 & I_q & 0 \\ Q^T & 0 & I_p \end{bmatrix} \begin{bmatrix} I_u & 0 & 0 \\ 0 & \hat{A} & -B \\ 0 & 0 & \alpha I_p \end{bmatrix} \begin{bmatrix} I_u & 0 & 0 \\ 0 & I_q & 0 \\ 0 & \frac{\gamma}{\alpha} B^T & I_p \end{bmatrix} \right)^{-1}. \tag{3.1}$$

Equation (3.1) shows that the RPF preconditioner can be effectively applied by solving a sequence of block triangular or diagonal systems. In particular, the matrices $\hat{K}$ and $\hat{A}$ of (2.10), along with the respective inverses, are required.

Such matrices depend on the relaxation parameter α. In particular, α^{-1} multiplies the rank-deficient matrices QQ^T and BB^T, which could prevail on K and A for small values of α. Hence, the accuracy and numerical stability in the computation of $\hat{K}^{-1}$ and $\hat{A}^{-1}$, or of their sparse approximations, depend on α. We now prove how the spectral condition numbers $\kappa_2(\hat{K})$ and $\kappa_2(\hat{A})$ increase for α approaching 0.

THEOREM 3.1. *Let C and FF^T be an SPD and a rank-deficient symmetric positive semidefinite (SPSD) matrix, respectively, with $\beta > 0$ a positive scalar. Then, the spectral condition number of $\hat{C} = C + \beta FF^T$ is such that*

$$\kappa_2(\hat{C}) \leq \omega_C(\beta)\kappa_2(C) \tag{3.2}$$

with $\omega_C(\beta) = 1 + \beta\lambda_1(S_C)$ and $S_C = F^T C^{-1} F$.

Proof. Let us factorize $\hat{C}$ as

$$\hat{C} = C^{\frac{1}{2}}\left(I + \beta C^{-\frac{1}{2}} FF^T C^{-\frac{1}{2}}\right) C^{\frac{1}{2}}, \tag{3.3}$$

where $C^{-\frac{1}{2}} FF^T C^{-\frac{1}{2}}$ is an SPSD matrix. Using the definition of condition number $\kappa_2(\hat{C}) = \|\hat{C}\|_2 \|\hat{C}^{-1}\|_2$ and the Cauchy–Schwarz inequality, we have

$$\kappa_2(\hat{C}) \leq \kappa_2(C^{\frac{1}{2}})\kappa_2(C^{\frac{1}{2}})\kappa_2(I + \beta C^{-\frac{1}{2}} FF^T C^{-\frac{1}{2}}), \tag{3.4}$$

and so

$$\frac{\kappa_2(\hat{C})}{\kappa_2(C)} \leq \frac{1 + \beta\lambda_1(C^{-\frac{1}{2}} FF^T C^{-\frac{1}{2}})}{1 + \beta\lambda_n(C^{-\frac{1}{2}} FF^T C^{-\frac{1}{2}})}, \tag{3.5}$$

where $\lambda_1(\cdot)$ and $\lambda_n(\cdot)$ denote the maximum and minimum eigenvalue in modulus of a matrix, respectively. Being $C^{-\frac{1}{2}} FF^T C^{-\frac{1}{2}}$ rank-deficient, $\lambda_n(C^{-1/2} FF^T C^{-1/2}) = 0$ and the nonzero eigenvalues are those of $F^T C^{-\frac{1}{2}} C^{-\frac{1}{2}} F$, i.e., S_C. Hence, we have

$$\kappa_2(\hat{C})\kappa_2(C)^{-1} \leq 1 + \beta\lambda_1(S_C). \tag{3.6}$$

∎

The result of Theorem 3.1 may be used to prescribe a lower bound to α in order to keep the condition number of $\hat{K}$ and $\hat{A}$ under control. Denoting as $\overline{\omega_K}$ and $\overline{\omega_A}$ the maximum user-specified acceptable value for ω_K and ω_A, we have

$$\alpha \geq \alpha_K = \frac{\lambda_1(S_K)}{\overline{\omega_K} - 1}, \qquad \alpha \geq \alpha_A = \frac{\gamma\lambda_1(\tilde{S}_A)}{\overline{\omega_A} - 1}, \tag{3.7}$$

where $\tilde{S}_A = \gamma^{-1} S_A$ is introduced to highlight the dependency of α_A on γ. Equations (3.7) provide two additional practical constraints for α in order to avoid numerical difficulties in the inversion of $\hat{K}$ and $\hat{A}$.

In summary, Figure 1 shows a brief sketch of the criteria used to select the optimal value of α as a function of γ, i.e., recalling (1.6d), ultimately of the time-step size Δt. The relaxation parameter must be larger than both α_K and $\|P\|_\infty$ for any value of γ. Typically, this constraint affects the selection α for $\gamma \to 0$, hence at the initial stages of a transient simulation where the time-step size is typically small. By distinction, for $\gamma \to \infty$, i.e., a large time-step size usually adopted toward the steady state, the value of α_A, which varies linearly with γ, becomes the most restrictive constraint. In the intermediate stages, α is selected using (2.24) or (2.35) and typically grows with γ.

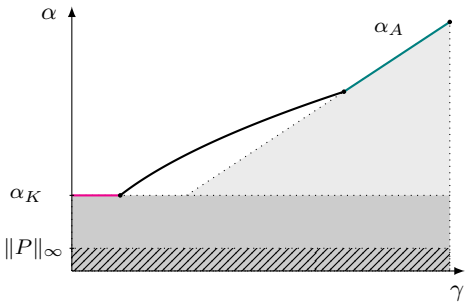

FIG. 1. *Sketch of the behavior of the relaxation parameter α versus γ.*

3.1. Implementation details. The computation of the RPF preconditioner $\mathbf{M}^{-1}$ can be subdivided into two stages. The first stage (Algorithm 3.1) involves only the γ-independent operations, which can be performed just once at the beginning of a full transient simulation and are regarded as a preprocessing cost. The second stage (Algorithm 3.2) computes the preconditioner components which vary at each time step.

Algorithm 3.1. RPF preconditioner computation: preprocessing stage.

if (fixed-stress) **then**
  $D_K = D_K^{(fs)}$
  $\lambda_1(D_K) = \|D_K\|_\infty$
else
  $D_K = Q^T \operatorname{diag}(K)^{-1} Q$
  Estimate $\lambda_1(D_K)$ using power-method
end if
$\tilde{D}_A = B^T \operatorname{diag}(\tilde{A})^{-1} B$
Estimate $\lambda_1(\tilde{D}_A)$ using power-method
$\alpha_K = (\overline{\omega_K} - 1)^{-1} \lambda_1(D_K)$
$\hat{K} = QQ^T$
$\hat{A} = BB^T$

Algorithm 3.2. RPF preconditioner computation.

if $\alpha = \alpha_1$ **then**
  Compute α using Newton–Raphson method
else if $\alpha = \alpha_2$ **then**
  $\alpha = (\sum_{i=n_P+1}^{n_p} \sqrt{D_K^{(i)} D_A^{(i)}} + n_P \|P\|_\infty)/n_p$
end if
$\alpha_A = (\overline{\omega_A} - 1)^{-1} \gamma \lambda_1(\tilde{D}_A)$
$\alpha \leftarrow \max\{\alpha, \alpha_K, \alpha_A\}$
$\hat{A} \leftarrow A + \gamma \alpha^{-1} \hat{A}$
$\hat{K} \leftarrow K + \alpha^{-1} \hat{K}$
Compute $M_{\hat{K}}^{-1}$ as a preconditioner for $\hat{K}$
Compute $M_{\hat{A}}^{-1}$ as a preconditioner for $\hat{A}$

Since the relaxation parameter α depends on γ, the local preconditioners for $\hat{K}$ and $\hat{A}$ have to be computed in the second stage, whenever γ varies. The computational cost of the preprocessing stage consists of the matrix-matrix products needed to compute QQ^T, BB^T, D_K, and $\tilde{D}_A$. The second stage relies on the computation of two sparse matrix merges and the preconditioners for $\hat{K}$ and $\hat{A}$.

Remark 3.2. Note that the nonzero pattern of QQ^T and BB^T is the same as K and A. Therefore, the sparse matrix-matrix products and merges can be performed trivially with no increase of memory occupation with respect to the original matrix blocks.

To apply the RPF preconditoner, i.e., computing $\mathbf{t} = \mathbf{M}^{-1}\mathbf{r}$ for some vector $\mathbf{r}$, we use again the factorization (3.1). The sequence of operations required to compute $\mathbf{t}^T = [\mathbf{t}_u^T, \mathbf{t}_q^T, \mathbf{t}_p^T]$ given the vector $\mathbf{r}^T = [\mathbf{r}_u^T, \mathbf{r}_q^T, \mathbf{r}_p^T]$ is summarized in Algorithm 3.3. Here we use the natural partition $\mathbf{t}_u, \mathbf{r}_u \in \mathbb{R}^{n_u}$, $\mathbf{t}_q, \mathbf{r}_q \in \mathbb{R}^{n_q}$, and $\mathbf{t}_p, \mathbf{r}_p \in \mathbb{R}^{n_p}$. The computational cost for applying the RPF preconditioner consists of two inner preconditioner applications, four matrix-vector products, and four vector updates.

Algorithm 3.3. RPF preconditioner application.

1: $\mathbf{x}_u = \alpha^{-1} Q \mathbf{r}_p$
2: $\mathbf{x}_u \leftarrow \mathbf{r}_u + \mathbf{x}_u$
3: **Apply** $M_{\hat{K}}^{-1}$ to $\mathbf{x}_u$ to get $\mathbf{t}_u$
4: $\mathbf{y}_p = Q^T \mathbf{t}_u$
5: $\mathbf{y}_p \leftarrow \mathbf{r}_p - \mathbf{y}_p$
6: $\mathbf{z}_q = B \mathbf{y}_p$
7: $\mathbf{z}_q \leftarrow \mathbf{r}_q + \alpha^{-1} \mathbf{z}_q$
8: **Apply** $M_{\hat{A}}^{-1}$ to $\mathbf{z}_q$ to get $\mathbf{t}_q$
9: $\mathbf{t}_p = B^T \mathbf{t}_q$
10: $\mathbf{t}_p \leftarrow \alpha^{-1} (\mathbf{y}_p - \gamma \mathbf{t}_p)$

The numerical experience also suggests that a preliminary diagonal scaling might be effective to ensure a better numerical balance and guarantee a similar accuracy for the different physical variables, i.e., displacement, velocity, and pressure in our case. Hence, a symmetric diagonal scaling of system $\mathbf{Ax} = \mathbf{b}$ is performed, i.e., $\mathbf{D}^{-1/2}\mathbf{A}\mathbf{D}^{-1/2}\mathbf{y} = \mathbf{D}^{-1/2}\mathbf{b}$, with $\mathbf{y} = \mathbf{D}^{1/2}\mathbf{x}$ and

$$\mathbf{D} = \begin{bmatrix} \operatorname{diag}(K) & 0 & 0 \\ 0 & \operatorname{diag}(A) & 0 \\ 0 & 0 & \operatorname{diag}(P) + \epsilon I_p \end{bmatrix}, \tag{3.8}$$

with $\epsilon = \eta / \max_i [\operatorname{diag}(K)]_i$, η being a user-specified parameter much smaller than 1, e.g., $\eta = 10^{-3}$. The selection of ϵ is done so as to ensure a proper numerical balancing even if the matrix P is null.

4. Numerical results. Two sets of numerical experiments are used to verify the preconditioner properties and effectiveness. The first set (Test 1) arises from Mandel's problem [45], i.e., a classic benchmark of linear poroelasticity. Herein the application of $\hat{K}^{-1}$ and $\hat{A}^{-1}$ is performed exactly via a nested direct solver. This problem is used to verify the theoretical properties of the preconditioner and test the accuracy of the optimal α estimate for a wide range of values of γ and the characteristic mesh size h. In the second set (Test 2), three real-world applications are considered in order

to check the robustness and efficiency of the preconditioner. Since the global size of the matrix $\mathbf{A}$ is here quite large, two incomplete Cholesky factorizations with a user-specified fill-in ρ_K and ρ_A [41] are used to apply inexactly $\hat{K}^{-1}$ and $\hat{A}^{-1}$, respectively. Of course, other potentially more efficient methods, e.g., multigrid techniques, could also be used. We recall (see (1.6d)) that the value of γ is proportional to the time-step size Δt used in the selected time-marching scheme. For the sake of simplicity, here we set $\gamma = \Delta t$ and in what follows we will discuss directly the effects of a Δt variation. In other words, a fully implicit backward Euler scheme is always used for time integration.

In all test cases, Bi-CGStab [53] is selected as a Krylov subspace method with the initial guess set to $\mathbf{M}^{-1}\mathbf{b}$. The iterations are stopped when the real relative residual falls below a user-specified tolerance τ. The computational performance is evaluated in terms of number of iterations n_{it} and CPU time in seconds for the preconditioner computation T_p (Algorithm 3.2) and for the solver to converge T_s. The total time is denoted by $T_t = T_p + T_s$. All computations are performed using a code written in Fortran 90 on an Intel Xeon CPU E5-1620 v4 at 3.5 GHz quad-core with 64 GB of RAM.

4.1. Test 1: Mandel's problem. This is a classical benchmark for validating coupled poromechanical models. The problem setup consists of a porous slab bounded by rigid, frictionless, impermeable plates. Side surfaces are stress-free, drained, and kept to ambient pressure at all times. At $t = 0$ the medium is suddenly subjected to a compressive force in the direction orthogonal to the confining plates (Figure 2), which produces an instantaneous constant pressure build-up along with a bilinear displacement field. For detailed information on the physical process, boundary and initial conditions, and the analytical solution, the reader can, for instance, refer to [22]. In our application, the problem domain, grid type, and physical and computational parameters are provided in Figure 2 and Table 1.

This test case has mainly a theoretical value and is used to investigate the properties of the RPF preconditioner. Therefore, we use a regular discretization grid whose characteristic size h is progressively refined as shown in Table 2 and apply the inverse of $\hat{K}$ and $\hat{A}$ exactly by means of an inner direct solver. The results are obtained setting $\Delta t/t_c = 10^{-3}$ and assuming an incompressible pore fluid ($\|P\|_\infty = 0$). The limiting values α_K and α_A/γ are obtained by setting $\overline{\omega_K} = 150$ and $\overline{\omega_A} = 650$.

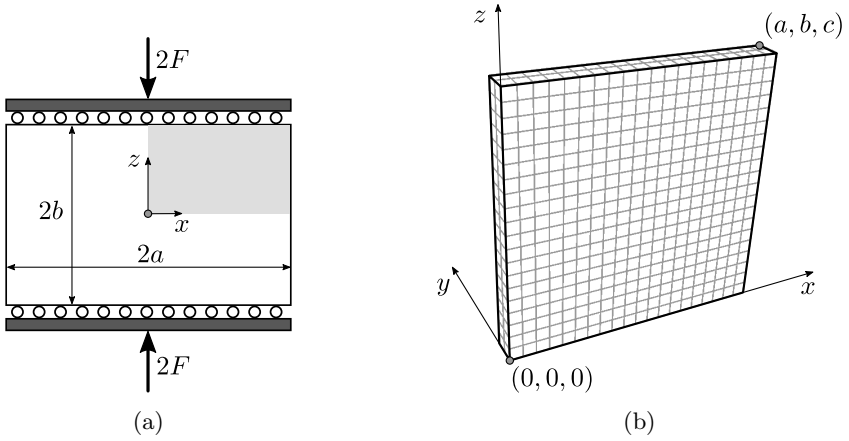

FIG. 2. *Test* 1*, Mandel's problem: sketch of the geometry* (a) *and the computational model* (b).

TABLE 1
Test 1, Mandel's problem: physical and computational parameters.

Quantity	Value	Unit
Young's modulus (E)	1×10^6	[Pa]
Poisson's ratio (ν)	0.2	[-]
Biot's coefficient (b)	1.0	[-]
Biot's modulus (M)	∞	[Pa]
Isotropic permeability (κ)	1×10^{-12}	[m^2]
Fluid viscosity (μ)	1×10^{-3}	[Pa $\cdot$ s]
Domain size x-z ($a = b$)	1.0	[m]
Domain size y (c)	0.1	[m]
Applied force magnitude ($\lvert F \rvert$)	2×10^2	[N $\cdot$ m^{-1}]
Characteristic consolidation time (t_c)	900	[s]
Solver tolerance (τ)	1×10^{-10}	[-]

TABLE 2
Test 1, Mandel's problem: block size and bounds to α.

a/h	n_u	n_q	n_p	$\|P\|_\infty$	α_K	α_A/γ
10	726	420	100	0.0	2.32×10^{-11}	6.46×10^{-12}
20	3,969	2,880	800	0.0	1.50×10^{-12}	3.96×10^{-12}
40	25,215	21,120	6,400	0.0	1.88×10^{-13}	2.26×10^{-12}
80	177,147	161,280	51,200	0.0	4.20×10^{-14}	1.18×10^{-12}

First of all, we study the dependency of the iteration count and the eigenspectrum of the preconditioned matrix on α. The results refer to the problem with $a/h = 10$. Figure 3(a) shows the number of iterations as a function of α and Figure 3(b) provides the eigenspectra of the preconditioned matrix for three values of α. The middle diagram is relative to the empirical value of α_{opt}, corresponding to the point with the minimum iteration count in Figure 3(a), whereas the top and the bottom diagrams are obtained for $\alpha < \alpha_{opt}$ and $\alpha > \alpha_{opt}$, respectively. As expected from Corollary 2.3, the eigenspectrum is real and bounded in $]0, 1]$. It can be noticed that when $\alpha > \alpha_{opt}$ the nonunitary eigenvalues are still clustered around a certain value, which is, however, getting closer to 0. Instead, when $\alpha < \alpha_{opt}$ the eigenvalues are less clustered, with the smallest one again approaching 0.

The results obtained by α estimated through the two different criteria (2.24) and (2.35), α_1 and α_2, respectively, are provided in Table 3. They are compared with the optimal value α_{opt} computed empirically from Figure 3(a), varying also Δt and h. Both estimates α_1 and α_2 are very close to the optimal one, with α_2 much easier to obtain.

The variation of the optimal α with the characteristic mesh size h is investigated in Table 4(a). According to (2.37), α_2 is expected to vary proportionally to $|\Gamma^{(e)}|$, i.e., h^2 in this case. This result is reproduced exactly in Table 4(a), where halving of the mesh size produces a reduction of one fourth of α. Table 4(b) compares the values of $\alpha_2/\sqrt{\gamma}$, i.e., the γ-independent part of α_2, computed using the different approximations $D_K^{(fs)}$ and D_K ((2.25) and (2.30)), for S_K. The two approaches produce similar estimates with the related iteration count actually unaffected by the choice.

The accuracy of the diagonal approximations of S_K and S_A in estimating the optimal α value can be observed in Figure 4(a), where the exact computation of $\mathrm{tr}[Z_\alpha]$ (analytic profile) is compared with the approximate formulation, achieved introducing the diagonal approximations D_A and D_K of (2.29) and (2.30). These results refer to the problem with $a/h = 10$. The two profiles turn out to be very close to each other. Notice also that in this case the function $\mathrm{tr}[Z_\alpha]$ has only one stationary point.

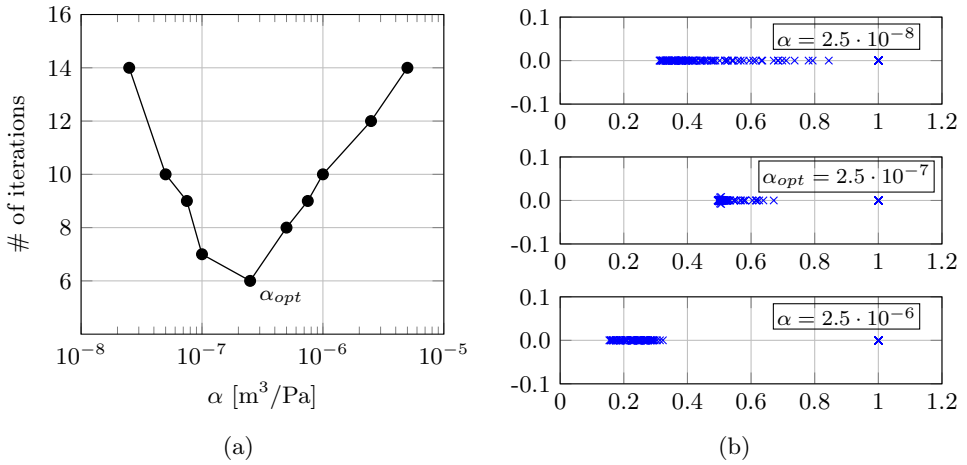

(a) (b)

FIG. 3. *Test* 1, *Mandel's problem* ($a/h = 10$)*: number of iterations versus* α (a) *and eigenspectrum for three values of* α (b).

TABLE 3

Test 1, *Mandel's problem: comparison between* α_1, α_2, *and* α_{opt} *by varying the mesh size* h *and time step* Δt *for the parameter set given in Table* 1.

a/h	$\Delta t/t_c$	α			n_{it}		
		α_1	α_2	α_{opt}	n_1	n_2	n_{opt}
10	10^{-6}	5.21×10^{-9}	5.29×10^{-9}	5.00×10^{-9}	4	4	4
	10^{-3}	1.65×10^{-7}	1.68×10^{-7}	2.50×10^{-7}	6	6	6
	10^{0}	5.21×10^{-6}	5.30×10^{-6}	1.00×10^{-6}	9	9	6
20	10^{-6}	5.41×10^{-10}	6.93×10^{-10}	5.00×10^{-10}	6	6	6
	10^{-3}	1.71×10^{-8}	2.19×10^{-8}	1.00×10^{-8}	8	8	7
	10^{0}	5.43×10^{-7}	6.93×10^{-7}	3.00×10^{-7}	12	12	10
40	10^{-6}	6.76×10^{-11}	8.64×10^{-11}	1.00×10^{-11}	7	7	6
	10^{-3}	2.14×10^{-9}	2.73×10^{-9}	1.50×10^{-9}	11	11	9
	10^{0}	6.77×10^{-8}	8.65×10^{-8}	4.00×10^{-8}	16	16	13
80	10^{-6}	1.08×10^{-11}	1.08×10^{-11}	7.50×10^{-12}	8	8	7
	10^{-3}	3.40×10^{-10}	3.41×10^{-10}	2.50×10^{-10}	18	18	16
	10^{0}	1.07×10^{-8}	1.08×10^{-8}	5.00×10^{-9}	24	24	18

However, this is not a general result and other problems where several different local maximum and minimum points are present can be built. Finally, Figure 4(b) provides the behavior of the ratios $\kappa_2(\hat{K})/\kappa_2(K)$ and $\kappa_2(\hat{A})/\kappa_2(A)$ versus α. As expected, the smaller the α, the more ill-conditioned $\hat{K}$ and $\hat{A}$, generating difficulties in the stable numerical application of their inverses. Theorem 3.1 provides an upper bound for such ill-conditioning increase through the introduction of the functions $\omega_K(\alpha)$ and $\omega_A(\alpha)$ (equation (3.7)). These bounds are also shown in Figure 4(b) and provide a good estimate of the actual $\hat{K}$ and $\hat{A}$ deterioration.

4.2. Test 2: Real-world applications. The performance of the RPF preconditioner is finally tested in three real-world applications dealing with coupled poromechanical problems typically related to the flow and deformation in geological media. Examples of such applications are the consolidation processes of shallow soils under a footing load or fluid withdrawal condition, which might result in the well-known

TABLE 4
Test 1*, Mandel's problem:* (a) *influence of mesh size* h *and* (b) S_K *approximation on* α_2.

a/h	$\alpha_2(h)/\alpha_2(2h)$		
	$\Delta t = 10^{-6}$	$\Delta t = 10^{-3}$	$\Delta t = 10^{0}$
10	-	-	-
20	0.260	0.261	0.262
40	0.251	0.249	0.249
80	0.249	0.249	0.249

(a)

a/h	$\alpha_2/\sqrt{\gamma}$	
	$D_K^{(fs)}$	D_K
10	1.3×10^{-7}	1.7×10^{-7}
20	1.8×10^{-8}	2.3×10^{-8}
40	2.3×10^{-9}	2.8×10^{-9}
80	2.8×10^{-10}	3.5×10^{-10}

(b)

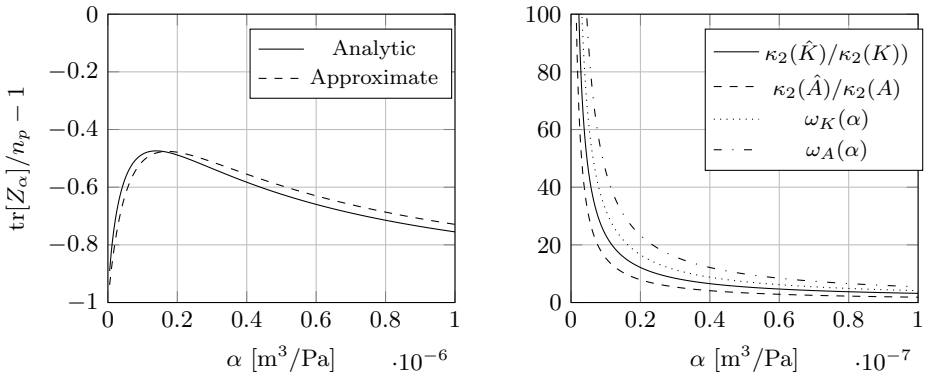

(a) (b)

FIG. 4. *Test* 1*, Mandel's problem* ($a/h = 10$)*:* $\mathrm{tr}\,[Z_\alpha]$ (a) *and* $\kappa_2(\hat{K})$, $\kappa_2(\hat{A})$, ω_K, ω_A (b) *versus* α.

phenomenon of land subsidence, e.g., [14, 15, 23]. Other important applications are related to petroleum engineering, e.g., [35, 37, 38], where the coupling occurs between the pore fluid flow and the deep reservoir geomechanics. These problems typically give rise to large-scale discrete models spanning long time intervals, where the inner system solution is often the most CPU-demanding task and the efficient design of the linear solver is a fundamental practical need. The test cases considered in this work are as follows:

- Test 2a: Treporti. The consolidation of a shallow formation due to the construction of a trial embankment is addressed. The simulation is based on the setup of a large-scale 5-year-long loading/unloading test aimed at characterizing the geomechanical properties of the sedimentary deposits at the Venice coastland in Italy. Alternating sandy, silty, and clayey layers down to 60-m depth are implemented according to the available stratigraphic information (Figure 5). For a detailed description of the experimental site, material properties, and boundary conditions, see [15, 16] and references therein.
- Test 2b: Chaobai. Land subsidence due to overexploitation of a shallow multiaquifer system is predicted in the Chaobai River alluvial fan in China. The study area is located in the Beijing Plain with an overall extent of 1,155 km^2. The strongly heterogeneous nature of the Chaobai River alluvial fan is accounted for with the aid of a statistical inverse framework in a multizone transition probability approach [56]. The results of a detailed reconstruction of the lithological heterogeneities down to an irregular rigid bedrock located

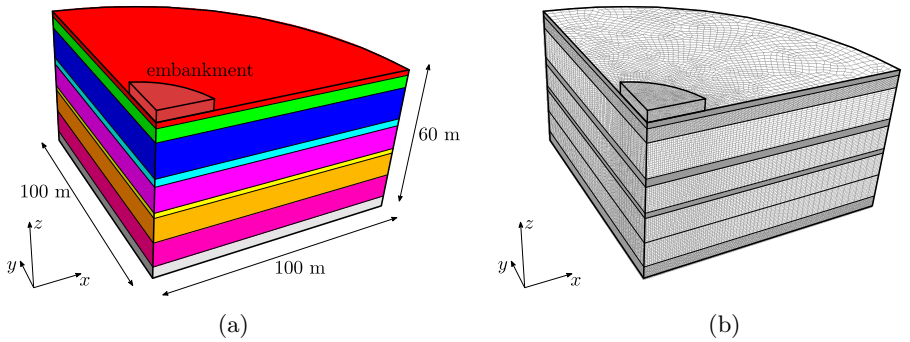

FIG. 5. *Test* 2a, *Treporti:* (a) *three-dimensional layered model domain and* (b) *computational model.*

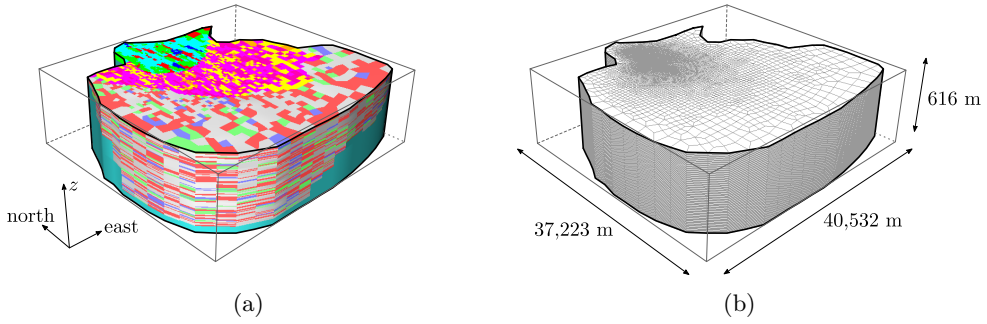

FIG. 6. *Test* 2b, *Chaobai:* (a) *lithofacies heterogeneous distribution in the porous domain and* (b) *three-dimensional discretization (modified from* [23]*).*

at about 550-m depth is used to distribute statistically the different faces in the simulated porous volume (Figure 6). Details on the model implementation are provided in [23].

- Test 2c: SPE10. We consider a well-driven flow in a deforming reservoir. The setup is based on the 10th SPE Comparative Solution Project [19] but is equipped with poroelastic mechanical behavior assuming incompressible fluid and solid constituents. We restrict the model to the top 35 layers, which are representative of a shallow-marine Tarbert formation characterized by severe permeability variations (Figure 7), namely, 8 and 12 orders of magnitude in the horizontal and vertical directions, respectively. The simulated domain covers an area of 365.76×650.56 m^2 and extends for 21.34 m in the vertical direction. The porous medium is populated with homogeneous elastic properties, namely, Young's modulus $E = 8.3{\times}10^3$ MPa, Poisson's ratio $\nu = 0.3$, and Biot's coefficient $b = 1.0$. The fluid viscosity is equal to 0.3×10^{-9} MPa·s. One injector and one production well, located at opposite corners of the domain, penetrate vertically the entire reservoir. Wells are modeled as line source according to a classical Peaceman model [47], which relates well control parameters, such as bottomhole pressure, to flow rates through the wellbore, assuming radial flow in the vicinity of the perforation. Additional details pertaining to well modeling in reservoir simulation can be found in [18].

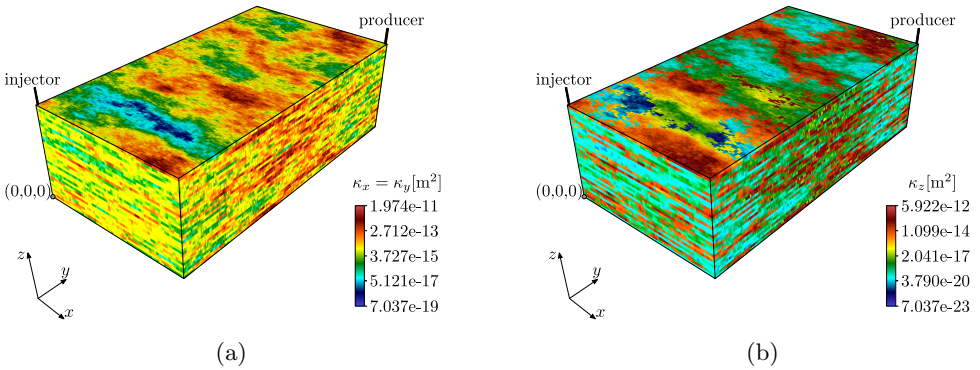

FIG. 7. *Test* 2c, *SPE*10*:* (a) *horizontal permeability* $\kappa_x = \kappa_y$ *and* (b) *vertical permeability* κ_z.

TABLE 5
Test 2*, real-world applications: size and number of nonzeros of the test matrices.*

Test	n_u	n_q	n_p	# nonzeros
2a: Treporti	1,379,385	1,345,444	442,944	90,192,580
2b: Chaobai	2,152,683	2,132,612	707,600	143,359,342
2c: SPE10	1,455,948	1,409,000	462,000	94,317,731

The size and number of nonzeros of the matrices arising from Test 2 are provided in Table 5.

4.2.1. Treporti. The performance of the RPF preconditioner is here considered for different values of the time-step size Δt. As mentioned, the application of $\hat{K}^{-1}$ and $\hat{A}^{-1}$ is carried out inexactly by an incomplete Cholesky decomposition with partial fill-in, ρ_K and ρ_A, respectively. Experimentally, the fill-in values giving the best results in this problem are $\rho_K = 50$ and $\rho_A = 10$. The results are provided in Table 6, where the performance obtained with the estimates α_1 and α_2 ((2.24) and (2.35), respectively) is compared to that of α_{opt}, which was estimated empirically by a trial-and-error procedure. The exit tolerance τ is set equal to 10^{-6}, whereas $\overline{\omega_K} = 45$ and $\overline{\omega_A} = 6000$. The bounds for α are $\|P\|_\infty = 0.0$ (incompressible fluid), $\alpha_K = 0.00052$, and $\alpha_A/\gamma = 0.00023$. The results show that both α_1 and α_2 are generally close to α_{opt}, though the latter is much cheaper to compute. Notice that, as expected from the analysis developed in section 3 and summarized in Figure 1, for small and large Δt the lower bounds α_K and α_A, respectively, can come into play. In any case, the proposed RPF preconditioner appears to be quite robust and able to address quite efficiently a large-size real-world problem.

For the sake of a comparison, Table 6 also shows the performance obtained on the same problem by the block triangular preconditioner (BTP) developed in [16]. This preconditioner is obtained by approximating the lower block triangular factor of $\mathbf{A}$ with the aid of local preconditioners for K and A and the fixed-stress strategy discussed in subsection 2.2 for the resulting Schur complement. Castelletto, White, and Ferronato [16] have shown the BTP robustness and efficiency in a number of test cases, with the main focus on its scalability with respect to the mesh size. As local preconditioners for K and A, we have used incomplete Cholesky decompositions to be consistent with the inner preconditioners for $\hat{K}$ and $\hat{A}$ employed with RPF. The fill-in values have been optimized with respect to the total CPU time T_t. The results

TABLE 6

Test 2a*, Treporti: iteration count and CPU times as a function of the time-step size and* α*. The average preconditioner computation time is equal to* 19.3 *seconds independently of* Δt*. A comparison with the BTP preconditioner* [16] *is also shown.*

	RPF				BTP		
Δt [day]	α	n_{it}	T_s [s]	T_t [s]	n_{it}	T_s [s]	T_t [s]
10^{-2}	$\alpha_1 = 0.00052$ (α_K)	85	80.9	101.8	91	115.15	152.3
	$\alpha_2 = 0.00059$	79	76.5	97.6			
	$\alpha_{opt} = 0.00055$	78	74.9	95.8			
10^{0}	$\alpha_1 = 0.0016$	51	49.4	69.9	64	82.10	119.5
	$\alpha_2 = 0.0034$	56	53.9	74.2			
	$\alpha_{opt} = 0.0010$	50	50.5	71.9			
10^{+2}	$\alpha_1 = 0.023$ (α_A)	87	83.3	103.8	63	79.4	116.8
	$\alpha_2 = 0.034$	63	60.1	80.2			
	$\alpha_{opt} = 0.035$	62	59.3	79.5			

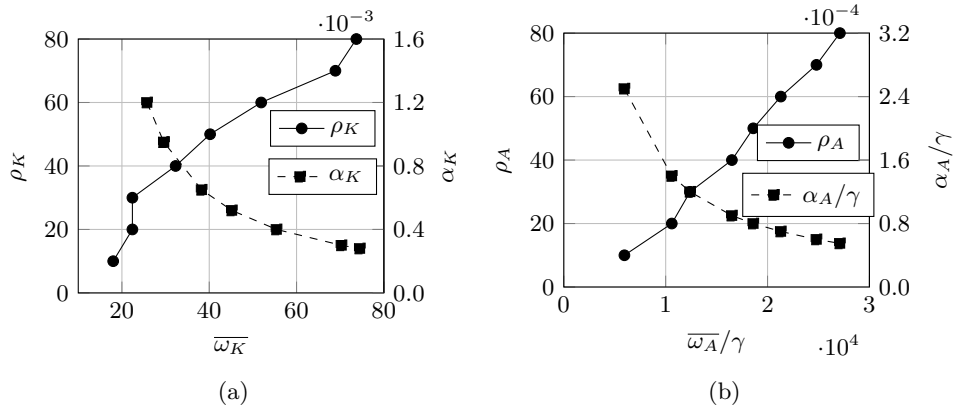

FIG. 8. *Test* 2a*, Treporti:* (a) ρ_K *and* α_K *versus* $\overline{\omega_K}$ *and* (b) ρ_A *and* α_A *versus* $\overline{\omega_A}/\gamma$.

of Table 6 show that in this test case the RPF preconditioner outperforms the BTP preconditioner, especially when small values of Δt are considered.

We use this test problem to investigate also the role played by the choice for the user-specified parameters $\overline{\omega_K}$ and $\overline{\omega_A}$ and their connection with the fill-in degree of $M_{\hat{K}}$ and $M_{\hat{A}}$, namely, ρ_K and ρ_A. Figure 8 shows how the required fill-in varies with $\overline{\omega_K}$ and $\overline{\omega_A}$ and the corresponding bounds α_K and α_A. Accepting larger values for $\overline{\omega_K}$ and $\overline{\omega_A}$, i.e., $\hat{K}$ and $\hat{A}$ are allowed to be more ill-conditioned, yields less restrictive bounds α_K and α_A, but this requires also a larger fill-in for $M_{\hat{K}}$ and $M_{\hat{A}}$. Of course, this can be detrimental for the overall RPF performance. Figure 8 shows also that generally $\overline{\omega_A}$ can be set larger to $\overline{\omega_K}$, though keeping the required value for ρ_A at an acceptable level. This is because A is often better conditioned than K.

The effect on the overall performance due to the selection of the fill-in degree is investigated in Figure 9, which shows the total CPU time as a function of ρ_K and ρ_A. The time step is set to $\Delta t = 1$ day in Figure 9(a) and $\Delta t = 1 \times 10^{-2}$ days in Figure 9(b). Using the lowest possible values for ρ_A appears to be the most convenient choice. On the other hand, the value of ρ_K has a slightly bigger impact on the preconditioner performance, but only if the estimate α_1 is used. In general, the RPF preconditioner appears to be quite robust to the selection of ρ_K.

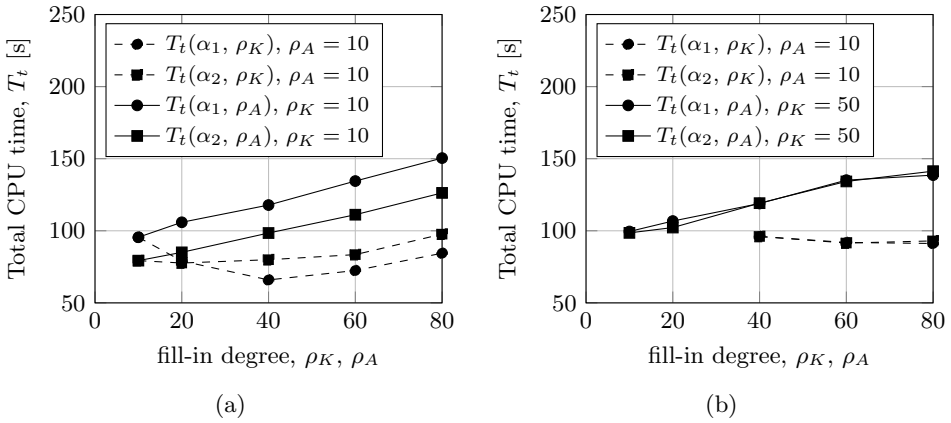

(a) (b)

FIG. 9. *Test* 2a, *Treporti: total CPU time versus fill-in degree for* (a) $\Delta t = 1$ *day and* (b) $\Delta t = 10^{-2}$ *days.*

TABLE 7

Test 2b, *Chaobai: iteration count and CPU times as a function of the time-step size and* α. *The average preconditioner computation time is* 59.3 *seconds. We set* $\overline{\omega_K} = 5.5$ *and* $\overline{\omega_A} = 1650.0$, *producing* $\alpha_K = 60.7$ *and* $\alpha_A/\gamma = 3958.5$. *The fill-in parameters* ρ_K *and* ρ_A *are set to* 60 *and* 50, *respectively.*

Δt [day]	α	n_{it}	T_s [s]	T_t [s]
10^{-3}	60.7 (α_K)	47	88.8	146.9
10^{-2}	177.3	46	92.5	156.1
10^{-1}	560.9	96	195.9	253.4
10^{0}	3958.5 (α_A)	173	332.1	386.6
10^{+1}	39585.1 (α_A)	205	389.1	446.4

TABLE 8

Test 2c, *SPE*10*: iteration count and CPU times as a function of the time-step size and* α. *The average preconditioner computation time is* 25.3 *seconds. We set* $\overline{\omega_K} = 20.7$ *and* $\overline{\omega_A} = 320.0$, *producing* $\alpha_K = 0.64$ *and* $\alpha_A/\gamma = 17.6$. *The fill-in parameters* ρ_K *and* ρ_A *are set to* 30 *and* 40, *respectively.*

Δt [day]	α	n_{it}	T_s [s]	T_t [s]
10^{-6}	0.0000301	63	64.2	88.1
10^{-4}	0.00176 (α_A)	57	60.4	84.9
10^{-2}	0.176 (α_A)	77	78.6	103.9
10^{0}	17.6 (α_A)	205	206.5	231.9

4.2.2. Chaobai and SPE10. The RPF preconditioner is finally tested in the real-world applications denoted as Chaobai and SPE10. Tables 7 and 8 provide the best performance for each problem over a wide range of Δt values. Based on the results discussed for Test 2a, the choice of two fill-in parameters, ρ_K and ρ_A, for the incomplete Cholesky factorizations of $\hat{K}$ and $\hat{A}$ is done by keeping the inner preconditioners as sparse as possible with respect to the selected $\overline{\omega_K}$ and $\overline{\omega_A}$ values. The exit tolerance τ is set equal to 10^{-6}.

Notice that these two applications are both characterized by a very pronounced heterogeneity, with significant jumps in the permeability field. For this reason, the inner block $\hat{A}$ is more ill-conditioned than in Test 2a, thus limiting the acceptable value for $\overline{\omega_A}$, especially in Test 2c, which is very severe in this sense, and reducing

the value of α_A. Nonetheless, convergence is always observed in all test problems with quite a satisfactory performance, especially on consideration of their size and ill-conditioning.

5. Conclusions. An RPF preconditioner is presented for coupled poromechanical models discretized with a mixed finite element formulation. The RPF preconditioner is inspired by the RDF successfully introduced for Navier–Stokes problems [6, 5] and can be derived for the problem at hand by introducing an appropriate splitting of the native 3×3 block matrix. The performance of the proposed preconditioner depends on the choice of the relaxation parameter α. From the analysis of the eigenspectrum of the preconditioned matrix, an optimal value for α is theoretically defined, along with a simple, stable, and inexpensive algorithm for its computation. Moreover, lower bounds for α are provided in order to keep the ill-conditioning of the inner blocks appearing in the RPF preconditioner, $\hat{K}$ and $\hat{A}$, under control. An extensive numerical experimentation, developed using both academic and real-world examples, shows the accuracy and stability of the estimate for the optimal relaxation parameter for different mesh and time-step sizes. In particular, in large-size real-world applications, characterized by strongly heterogeneous media, the RPF preconditioner proves very robust and efficient, thus being a promising alternative for the efficient monolithic solution to mixed finite element coupled poromechanics.

Appendix A. Derivation of M_1^{-1} and M_2^{-1}. Let us write M_1^{-1} and M_2^{-1} in the following form:

$$M_1^{-1} = \begin{bmatrix} X & 0 & W \\ 0 & \frac{1}{\alpha} I_q & 0 \\ Z & 0 & Y \end{bmatrix}, \quad M_2^{-1} = \begin{bmatrix} \frac{1}{\alpha} I_u & 0 & 0 \\ 0 & X' & W' \\ 0 & Z' & Y' \end{bmatrix} \tag{A.1}$$

with X, Y, W, Z, X', Y', W', and Z' blocks of the appropriate size. The products $M_1 M_1^{-1}$ and $M_2 M_2^{-1}$ must equate the identity:

$$M_1 M_1^{-1} = \begin{bmatrix} K & 0 & -Q \\ 0 & \alpha I_q & 0 \\ Q^T & 0 & \alpha I_p \end{bmatrix} \begin{bmatrix} X & 0 & W \\ 0 & \frac{1}{\alpha} I_q & 0 \\ Z & 0 & Y \end{bmatrix} = \begin{bmatrix} I_u & 0 & 0 \\ 0 & I_q & 0 \\ 0 & 0 & I_p \end{bmatrix}, \tag{A.2}$$

$$M_2 M_2^{-1} = \begin{bmatrix} \alpha I_u & 0 & 0 \\ 0 & A & -B \\ 0 & \gamma B^T & \alpha I_p \end{bmatrix} \begin{bmatrix} \frac{1}{\alpha} I_u & 0 & 0 \\ 0 & X' & W' \\ 0 & Z' & Y' \end{bmatrix} = \begin{bmatrix} I_u & 0 & 0 \\ 0 & I_q & 0 \\ 0 & 0 & I_p \end{bmatrix}. \tag{A.3}$$

From (A.2) and (A.3), the following conditions hold:

$$\begin{cases} KX - QZ = I_u, \\ Q^T X + \alpha Z = 0, \\ KW - QY = 0, \\ Q^T W + \alpha Y = I_p, \end{cases} \qquad \begin{cases} AX' - BZ' = I_q, \\ \gamma B^T X' + \alpha Z' = 0, \\ AW' - BY' = 0, \\ \gamma B^T W' + \alpha Y' = I_p. \end{cases} \tag{A.4}$$

From the second equations in (A.4), it's possible to obtain Z and Z',

$$Z = -\frac{1}{\alpha} Q^T X, \qquad Z' = -\frac{\gamma}{\alpha} B^T X', \tag{A.5}$$

which introduced in the first equations provide, assuming that $\hat{K}$ and $\hat{A}$ are regular matrices,

$$X = \hat{K}^{-1}, \qquad X' = \hat{A}^{-1}. \tag{A.6}$$

Similarly, Y and Y' can be obtained from the fourth equations of (A.4),

$$Y = \frac{1}{\alpha}(I_p - Q^T W), \qquad Y' = \frac{1}{\alpha}(I_p - \gamma B^T W'), \tag{A.7}$$

and replaced into the third equations give

$$W = \frac{1}{\alpha}\hat{K}^{-1}Q, \qquad W' = \frac{1}{\alpha}\hat{A}^{-1}B. \tag{A.8}$$

Finally, putting together all the equations above, the matrices M_1^{-1} and M_2^{-1} read

(A.9)
$$\mathbf{M}_1^{-1} = \frac{1}{\alpha}\begin{bmatrix} \alpha\hat{K}^{-1} & 0 & \hat{K}^{-1}Q \\ 0 & I_q & 0 \\ -Q^T\hat{K}^{-1} & 0 & I_p - \frac{1}{\alpha}\hat{S}_K \end{bmatrix}, \quad \mathbf{M}_2^{-1} = \frac{1}{\alpha}\begin{bmatrix} I_u & 0 & 0 \\ 0 & \alpha\hat{A}^{-1} & \hat{A}^{-1}B \\ 0 & -\gamma B^T\hat{A}^{-1} & I_p - \frac{1}{\alpha}\hat{S}_A \end{bmatrix}.$$

Appendix B. Derivation of Z_α. To obtain the expression of Z_α of (2.18), we first prove the following simple commutation relationships.

LEMMA B.1. *Let $S_K = Q^T K^{-1} Q$ and $S_A = \gamma B^T A^{-1} B$. Then*

$$\hat{S}_K = \alpha S_K \left(\alpha I_p + S_K\right)^{-1} = \alpha \left(\alpha I_p + S_K\right)^{-1} S_K, \tag{B.1a}$$

$$\hat{S}_A = \alpha S_A \left(\alpha I_p + S_A\right)^{-1} = \alpha \left(\alpha I_p + S_A\right)^{-1} S_A. \tag{B.1b}$$

Proof. Let us prove the first equality in (B.1a),

$$\begin{aligned} S_K = Q^T K^{-1} Q &= Q^T K^{-1} \left(I_u + \frac{1}{\alpha} Q Q^T K^{-1}\right)^{-1} \left(I_u + \frac{1}{\alpha} Q Q^T K^{-1}\right) Q \\ &= \frac{1}{\alpha} Q^T \left(K + \frac{1}{\alpha} Q Q^T\right)^{-1} Q \left(\alpha I_p + Q^T K^{-1} Q\right) = \frac{1}{\alpha}\hat{S}_K \left(\alpha I_p + S_K\right), \end{aligned} \tag{B.2}$$

and likely for the second equality,

$$\begin{aligned} S_K = Q^T &\left(I_u + \frac{1}{\alpha} K^{-1} Q Q^T\right) \left(I_u + \frac{1}{\alpha} K^{-1} Q Q^T\right)^{-1} K^{-1} Q \\ &= \frac{1}{\alpha}\left(\alpha I_p + Q^T K^{-1} Q\right) Q^T \left(K + \frac{1}{\alpha} Q Q^T\right)^{-1} Q = \frac{1}{\alpha}\left(\alpha I_p + S_K\right)\hat{S}_K. \end{aligned} \tag{B.3}$$

Proceeding likewise, the equalities in (B.1b) can be easily proved as well. First,

$$\begin{aligned} S_A = \gamma B^T A^{-1} B &= \gamma B^T A^{-1} \left(I_q + \frac{\gamma}{\alpha} B B^T A^{-1}\right)^{-1} \left(I_q + \frac{\gamma}{\alpha} B B^T A^{-1}\right) B \\ &= \frac{\gamma}{\alpha} B^T \left(A + \frac{\gamma}{\alpha} B B^T\right)^{-1} B \left(\alpha I_p + \gamma B^T A^{-1} B\right) = \frac{1}{\alpha}\hat{S}_A \left(\alpha I_p + S_A\right), \end{aligned} \tag{B.4}$$

and then

$$\begin{aligned} S_A = \gamma B^T &\left(I_q + \frac{\gamma}{\alpha} A^{-1} B B^T\right) \left(I_q + \frac{\gamma}{\alpha} A^{-1} B B^T\right)^{-1} A^{-1} B \\ &= \frac{\gamma}{\alpha}\left(\alpha I_p + \gamma B^T A^{-1} B\right) B^T \left(A + \frac{\gamma}{\alpha} B B^T\right)^{-1} B = \frac{1}{\alpha}\left(\alpha I_p + S_A\right)\hat{S}_A. \end{aligned} \tag{B.5}$$

∎

Now, Z_α of (2.11) can be rewritten in an equivalent form by introducing the commutation relationships of Lemma B.1:

(B.6)
$$\begin{aligned} Z_\alpha = \frac{1}{\alpha}\left[\alpha S_K\left(\alpha I_p + S_K\right)^{-1} + P + \alpha S_A\left(\alpha I_p + S_A\right)^{-1}\right] - \frac{1}{\alpha^2}\Big[2\alpha^2 S_K\left(\alpha I_p + S_K\right)^{-1} \\ S_A\left(\alpha I_p + S_A\right)^{-1} + \alpha S_K\left(\alpha I_p + S_K\right)^{-1} P + \alpha P S_A\left(\alpha I_p + S_A\right)^{-1}\Big] \\ + \frac{1}{\alpha^3}\left[\alpha S_K\left(\alpha I_p + S_K\right)^{-1} P \alpha S_A\left(\alpha I_p + S_A\right)^{-1}\right]. \end{aligned}$$

Gathering $(\alpha I_p + S_K)^{-1}$ on the left and $(\alpha I_p + S_A)^{-1}$ on the right, we have

(B.7)
$$\begin{aligned} Z_\alpha &= S_K\left(\alpha I_p + S_K\right)^{-1}\left[I_p - 2S_A\left(\alpha I_p + S_A\right)^{-1} - \frac{P}{\alpha} + \frac{P}{\alpha} S_A\left(\alpha I_p + S_A\right)^{-1}\right] \\ &\quad + \left[S_A + \frac{P}{\alpha}\left(\alpha I_p + S_A\right) - \frac{P}{\alpha} S_A\right]\left(\alpha I_p + S_A\right)^{-1} \\ &= S_K\left(\alpha I_p + S_K\right)^{-1}\left[\left(\alpha I_p - S_A - P\right)\left(\alpha I_p + S_A\right)^{-1}\right] + \left[S_A + P\right]\left(\alpha I_p + S_A\right)^{-1} \\ &= \left[S_K\left(\alpha I_p + S_K\right)^{-1}\left(\alpha I_p - S_A - P\right) + \left(S_A + P\right)\right]\left(\alpha I_p + S_A\right)^{-1}. \end{aligned}$$

Finally, exploiting the commutation property given by (B.2), the factors order of the product $S_K(\alpha I_p + S_K)^{-1}$ can be swapped:

(B.8)
$$\begin{aligned} Z_\alpha &= \left[\left(\alpha I_p + S_K\right)^{-1} S_K\left(\alpha I_p - S_A - P\right) + \left(S_A + P\right)\right]\left(\alpha I_p + S_A\right)^{-1} \\ &= \Big[\left(\alpha I_p + S_K\right)^{-1} S_K\left(\alpha I_p - S_A - P\right) \\ &\quad + \left(\alpha I_p + S_K\right)^{-1}\left(\alpha I_p + S_K\right)\left(S_A + P\right)\Big]\left(\alpha I_p + S_A\right)^{-1}. \end{aligned}$$

In this way, finally Z_α reads

(B.9)
$$\begin{aligned} Z_\alpha &= \left(\alpha I_p + S_K\right)^{-1}\left[S_K\left(\alpha I_p - S_A - P\right) + \left(\alpha I_p + S_K\right)\left(S_A + P\right)\right]\left(\alpha I_p + S_A\right)^{-1} \\ &= \alpha\left(\alpha I_p + S_K\right)^{-1}(P + S_K + S_A)(\alpha I_p + S_A)^{-1} = \alpha\left(\alpha I_p + S_K\right)^{-1} S(\alpha I_p + S_A)^{-1}. \end{aligned}$$

REFERENCES

[1] J. H. Adler, F. J. Gaspar, X. Hu, C. Rodrigo, and L. T. Zikatanov, *Robust block preconditioners for Biot's model*, in Domain Decomposition Methods in Science and Engineering XXIV, P. E. Bjøstad, S. C. Brenner, L. Halpern, H. H. Kim, R. Kornhuber, T. Rahman, and O. B. Widlund, eds., Lect. Notes Comput. Sci. Eng. 125, Springer, New York, 2018, pp. 3–16, https://doi.org/10.1007/978-3-319-93873-8.

[2] T. Almani, K. Kumar, A. Dogru, G. Singh, and M. F. Wheeler, *Convergence analysis of multirate fixed-stress split interative schemes for coupling flow with geomechanics*, Comput. Methods Appl. Mech. Engrg., 311 (2016), pp. 180–207, https://doi.org/10.1016/j.cma.2016.07.036.

[3] O. Axelsson, R. Blaheta, and P. Byczanski, *Stable discretization of poroelasticity problems and efficient preconditioners for arising saddle point type matrices*, Comput. Vis. Sci., 15 (2012), pp. 191–207, https://doi.org/10.1007/s00791-013-0209-0.

[4] M. Bause, F. A. Radu, and U. Köcher, *Space–time finite element approximation of the Biot poroelasticity system with iterative coupling*, Comput. Methods Appl. Mech. Engrg., 320 (2017), pp. 745–768, https://doi.org/10.1016/j.cma.2017.03.017.

[5] M. Benzi, S. Deparis, G. Grandperrin, and A. Quarteroni, *Parameter estimates for the Relaxed Dimensional Factorization preconditioner and application to hemodynamics*, Comput. Methods Appl. Mech. Engrg., 300 (2016), pp. 129–145, https://doi.org/10.1016/j.cma.2015.11.016.

[6] M. Benzi, M. Ng, Q. Niu, and Z. Wang, *A Relaxed Dimensional Factorization preconditioner for the incompressible Navier-Stokes equations*, J. Comput. Phys., 230 (2011), pp. 6185–6202, https://doi.org/10.1016/j.jcp.2011.04.001.

[7] L. Bergamaschi, M. Ferronato, and G. Gambolati, *Novel preconditioners for the iterative solution to FE-discretized coupled consolidation equations*, Comput. Methods Appl. Mech. Engrg., 196 (2007), pp. 2647–2656, https://doi.org/10.1016/j.cma.2007.01.013.

[8] L. Bergamaschi, S. Mantica, and G. Manzini, *A mixed finite element-finite volume formulation of the black oil model*, SIAM J. Sci. Comput., 20 (1998), pp. 970–997, https://doi.org/10.1137/S1064827595289303.

[9] L. Bergamaschi and Á. Martínez, *RMCP: Relaxed Mixed Constraint Preconditioners for saddle point linear systems arising in geomechanics*, Comput. Methods Appl. Mech. Engrg., 221–222 (2012), pp. 54–62, https://doi.org/10.1016/j.cma.2012.02.004.

[10] M. A. Biot, *General theory of three-dimensional consolidation*, J. Appl. Phys., 12 (1941), pp. 155–164, https://doi.org/10.1063/1.1712886.

[11] M. Borregales, F. A. Radu, K. Kumar, and J. M. Nordbotten, *Robust iterative schemes for non-linear poromechanics*, Comput. Geosci., 22 (2018), pp. 1021–1038, https://doi.org/10.1007/s10596-018-9736-6.

[12] J. W. Both, M. Borregales, J. M. Nordbotten, K. Kumar, and F. A. Radu, *Robust fixed stress splitting for Biot's equations in heterogeneous media*, Appl. Math. Lett., 68 (2017), pp. 101–108, https://doi.org/10.1016/j.aml.2016.12.019.

[13] J. W. Both, K. Kumar, J. M. Nordbotten, and F. A. Radu, *Anderson accelerated fixed-stress splitting schemes for consolidation of unsaturated porous media*, Comput. Math. Appl., 77 (2019), pp. 1479–1502, https://doi.org/10.1016/j.camwa.2018.07.033.

[14] N. Castelletto, M. Ferronato, and G. Gambolati, *Thermo-hydro-mechanical modeling of fluid geological storage by Godunov-mixed methods*, Internat. J. Numer. Meth. Engrg., 90 (2012), pp. 988–1009, https://doi.org/10.1002/nme.3352.

[15] N. Castelletto, G. Gambolati, and P. Teatini, *A coupled MFE poromechanical model of a large-scale load experiment at the coastland of Venice*, Comput. Geosci., 19 (2015), pp. 17–29, https://doi.org/10.1007/s10596-014-9450-y.

[16] N. Castelletto, J. A. White, and M. Ferronato, *Scalable algorithms for three-field mixed finite element coupled poromechanics*, J. Comput. Phys., 327 (2016), pp. 894–918, https://doi.org/10.1016/j.jcp.2016.09.063.

[17] X. Chen, K. K. Phoon, and K. C. Toh, *Partitioned versus global Krylov subspace iterative methods for FE solution of 3-D Biot's problem*, Comput. Methods Appl. Mech. Engrg., 196 (2007), pp. 2737–2750, https://doi.org/10.1016/j.cma.2007.02.003.

[18] Z. Chen, G. Huan, and Y. Ma, *Computational Methods for Multiphase Flows in Porous*, Comput. Sci. Eng. 2, SIAM, Philadelphia, 2006.

[19] M. A. Christie and M. J. Blunt, *Tenth SPE comparative solution project: A comparison of upscaling techniques*, SPE Reserv. Eval. Eng., 4 (2001), pp. 308–317, https://doi.org/10.2118/72469-PA.

[20] S. Dana, B. Ganis, and M. F. Wheeler, *A multiscale fixed stress split iterative scheme for coupled flow and poromechanics in deep subsurface reservoirs*, J. Comput. Phys., 352 (2018), pp. 1–22, https://doi.org/10.1016/j.jcp.2017.09.049.

[21] S. Dana and M. F. Wheeler, *Convergence analysis of two-grid fixed stress split iterative scheme for coupled flow and deformation in heterogeneous poroelastic media*, Comput. Methods Appl. Mech. Engrg., 341 (2018), pp. 788–806, https://doi.org/10.1016/j.cma.2018.07.018.

[22] M. Ferronato, N. Castelletto, and G. Gambolati, *A fully coupled 3-D mixed finite element model of Biot consolidation*, J. Comput. Phys., 229 (2010), pp. 4813–4830, https://doi.org/10.1016/j.jcp.2010.03.018.

[23] M. Ferronato, L. Gazzola, N. Castelletto, P. Teatini, and L. Zhu, *A coupled Mixed Finite Element Biot model for land subsidence prediction in the Beijing area*, in Poromechanics VI, M. Vandamme, P. Dangla, J.-M. Pereira, and S. Ghabezloo, eds., American Society of Civil Engineers, 2017, pp. 182–189, https://doi.org/10.1061/9780784480779.022.

[24] M. Ferronato, G. Pini, and G. Gambolati, *The role of preconditioning in the solution to FE coupled consolidation equations by Krylov subspace methods*, Int. J. Numer. Anal. Methods Geomech., 33 (2009), pp. 405–423, https://doi.org/10.1002/nag.729.

[25] A. J. H. Frijns, *A Four-Component Mixture Theory Applied to Cartilaginous Tissues: Numerical Modelling and Experiments*, Ph.D. thesis, Technische Universiteit Eindhoven, The Netherlands, 2000.

[26] F. J. Gaspar, F. J. Lisbona, C. W. Oosterlee, and R. Wienands, *A systematic comparison of coupled and distributive smoothing in multigrid for the poroelasticity system*, Numer. Linear Algebra Appl., 11 (2004), pp. 93–113, https://doi.org/10.1002/nla.372.

[27] F. J. Gaspar and C. Rodrigo, *On the fixed-stress split scheme as smoother in multigrid methods for coupling flow and geomechanics*, Comput. Methods Appl. Mech. Engrg., 326 (2017), pp. 526–540, https://doi.org/10.1016/j.cma.2017.08.025.

[28] V. Girault, K. Kumar, and M. F. Wheeler, *Convergence of iterative coupling of geomechanics with flow in a fractured poroelastic medium*, Comput. Geosci., 20 (2016), pp. 997–1011, https://doi.org/10.1007/s10596-016-9573-4.

[29] J. B. Haga, H. Osnes, and H. P. Langtangen, *A parallel block preconditioner for large-scale poroelasticity with highly heterogeneous material parameters*, Comput. Geosci., 16 (2012), pp. 723–734, https://doi.org/10.1007/s10596-012-9284-4.

[30] J. B. Haga, H. Osnes, and H. P. Langtangen, *On the causes of pressure oscillations in low-permeable and low-compressible porous media*, Int. J. Numer. Anal. Methods Geomech., 36 (2012), pp. 1507–1522, https://doi.org/10.1002/nag.1062.

[31] Q. Hong and J. Kraus, *Parameter-robust stability of classical three-field formulation of Biot's consolidation model*, Electron. Trans. Numer. Anal., 48 (2018), pp. 202–226, https://doi.org/10.1553/etna_vol48s202.

[32] Q. Hong, J. Kraus, M. Lymbery, and M. F. Wheeler, *Parameter-Robust Convergence Analysis of Fixed-Stress Split Iterative Method for Multiple-Permeability Poroelasticity Systems*, arXiv:1812.11809, 2018.

[33] R. A. Horn and C. R. Johnson, *Matrix Analysis*, 2nd ed., Cambridge University Press, New York, 2013.

[34] X. Hu, C. Rodrigo, F. J. Gaspar, and L. T. Zikatanov, *A nonconforming finite element method for the Biot's consolidation model in poroelasticity*, J. Comput. Appl. Math., 310 (2017), pp. 143–154, https://doi.org/10.1016/j.cam.2016.06.003.

[35] B. Jha and R. Juanes, *A locally conservative finite element framework for the simulation of coupled flow and reservoir geomechanics*, Acta Geotech., 2 (2007), pp. 139–153, https://doi.org/10.1007/s11440-007-0033-0.

[36] B. Jha and R. Juanes, *Coupled multiphase flow and poromechanics: A computational model of pore pressure effects on fault slip and earthquake triggering*, Water Resources Res., 5 (2014), pp. 3776–3808, https://doi.org/10.1002/2013WR015175.

[37] J. Kim, H. A. Tchelepi, and R. Juanes, *Stability, accuracy and efficiency of sequential methods for coupled flow and geomechanics*, SPE J., 16 (2011), pp. 249–262, https://doi.org/10.2118/119084-PA.

[38] J. Kim, H. A. Tchelepi, and R. Juanes, *Stability and convergence of sequential methods for coupled flow and geomechanics: Fixed-stress and fixed-strain splits*, Comput. Methods Appl. Mech. Engrg., 200 (2011), pp. 1591–1606, https://doi.org/10.1016/j.cma.2010.12.022.

[39] Y. Kuznetsov, K. Lipnikov, S. Lyons, and S. Maliassov, *Mathematical modeling and numerical algorithms for poroelastic problems*, in Current Trends in Scientific Computing, Z. Chen, R. Glowinski, and K. Li, eds., Contemp. Math. 329, AMS, Providence, RI, 2003, pp. 191–202, https://dx.doi.org/10.1090/conm/329.

[40] J. J. Lee, K.-A. Mardal, and R. Winther, *Parameter-robust discretization and preconditioning of Biot's consolidation model*, SIAM J. Sci. Comput., 39 (2017), pp. A1–A24, https://doi.org/10.1137/15M1029473.

[41] C.-J. Lin and J. J. Moré, *Incomplete Cholesky factorizations with limited memory*, SIAM J. Sci. Comput., 21 (1999), pp. 24–45, https://doi.org/10.1137/S1064827597327334.

[42] K. Lipnikov, *Numerical Methods for the Biot Model in Poroelasticity*, Ph.D. thesis, University of Houston, 2002.

[43] P. Luo, C. Rodrigo, F. J. Gaspar, and C. W. Oosterlee, *Multigrid method for nonlinear poroelasticity equations*, Comput. Visual Sci., 17 (2015), pp. 255–265, https://doi.org/10.1007/s00791-016-0260-8.

[44] P. Luo, C. Rodrigo, F. J. Gaspar, and C. W. Oosterlee, *On an Uzawa smoother in multigrid for poroelasticity equations*, Numer. Linear Algebra Appl., 24 (2017), e2074, https://doi.org/10.1002/nla.2074.

[45] J. Mandel, *Consolidation des sols (Étude mathématique)*, Geotechnique, 3 (1953), pp. 287–299, https://doi.org/10.1680/geot.1953.3.7.287.

[46] A. Mikelič and M. F. Wheeler, *Convergence of iterative coupling for coupled flow and geomechanics*, Comput. Geosci., 17 (2013), pp. 455–461, https://doi.org/10.1007/s10596-012-9318-y.

[47] D. W. Peaceman, *Interpretation of well-block pressures in numerical reservoir simulation*, SPE J., 18 (1978), pp. 183–194, https://doi.org/10.2118/6893-PA.

[48] P. J. Phillips and M. F. Wheeler, *A coupling of mixed and continuous Galerkin finite element methods for poroelasticity* I*: The continuous in time case*, Comput. Geosci., 11 (2007), pp. 131–144, https://doi.org/10.1007/s10596-007-9045-y.

[49] P. J. Phillips and M. F. Wheeler, *A coupling of mixed and continuous Galerkin finite element methods for poroelasticity* II*: The discrete-in-time case*, Comput. Geosci., 11 (2007), pp. 145–158, https://doi.org/10.1007/s10596-007-9044-z.

[50] K. K. Phoon, K. C. Toh, S. H. Chan, and F. H. Lee, *An efficient diagonal preconditioner for finite element solution of Biot's consolidation equations*, Internat. J. Numer. Methods Engrg., 55 (2002), pp. 377–400, https://doi.org/10.1002/nme.500.

[51] C. Rodrigo, X. Hu, P. Ohm, J. H. Adler, F. J. Gaspar, and L. T. Zikatanov, *New stabilized discretizations for poroelasticity and the Stokes' equations*, Comput. Methods Appl. Mech. Engrg., 341 (2018), pp. 467–484, https://doi.org/10.1016/j.cma.2018.07.003.

[52] E. Turan and P. Arbenz, *Large scale micro finite element analysis of* 3*D bone poroelasticity*, Parallel Comput., 40 (2014), pp. 239–250, https://doi.org/10.1016/j.parco.2013.09.002.

[53] H. A. Van der Vorst, *Bi-CGSTAB: A fast and smoothly converging variant of Bi-CG for the solution of nonsymmetric linear systems*, SIAM J. Sci. Stat. Comput., 13 (1992), pp. 631–644, https://doi.org/10.1137/0913035.

[54] J. A. White and R. I. Borja, *Block-preconditioned Newton–Krylov solvers for fully coupled flow and geomechanics*, Comput. Geosci., 15 (2011), pp. 647–659, https://doi.org/10.1007/s10596-011-9233-7.

[55] J. A. White, N. Castelletto, and H. A. Tchelepi, *Block-partitioned solvers for coupled poromechanics: A unified framework*, Comput. Methods Appl. Mech. Engrg., 303 (2016), pp. 55–74, https://doi.org/10.1016/j.cma.2016.01.008.

[56] L. Zhu, Z. Dai, H. Gong, C. Gable, and P. Teatini, *Statistic inversion of multi-zone transition probability models for aquifer characterization in alluvial fans*, Stoch. Environ. Res. Risk Assessment, 30 (2016), pp. 1005–1016, https://doi.org/10.1007/s00477-015-1089-2.